This manuscript is a preprint and plan to be submitted for publication in **Basin Research**. Please note that this manuscript has not yet undergone peer-review; as such, subsequent version of this manuscript may have different content. We invite you to contact any of the authors directly to comment and give any feedbacks on the manuscripts.

DEFORMATION OF A SHALE-DOMINATED DELTA: TARAKAN BASIN, OFFSHORE INDONESIA

Aurio Erdi[1,2], Christopher A-L. Jackson[1], Juan I. Soto[3,#]

[1]*Basin Research Group (BRG), Department of Earth Science and Engineering, Imperial College, London, United Kingdom*

[2]*National Research and Innovation Agency (BRIN), Indonesia*

[3]*Bureau of Economic Geology, Jackson School of Geosciences, The University of Texas at Austin, University Station, Box X, Austin, Texas, 78713-8924, USA*

[#]*On leave of absence from: Departamento de Geodinámica, Universidad de Granada, Avenida de Fuente Nueva s/n, 18071 Granada, Spain*

Corresponding author:
Aurio Erdi, Basin Research Group (BRG), Department of Earth Science and Engineering, Imperial College, Prince Consort Road, London, S W7 2BP, United Kingdom.
Email: a.erdi18@imperial.ac.uk

Abstract

Deformation on shale-rich continental margins is commonly associated with thin-skinned extension above mobile shales. Normal faulting and shale mobilization are widespread on such margins, being associated with and controlled by progradation and gravitational failure of deltaic sedimentary wedges. However, due to limitations in our ability to seismically imaging these mobile shales, our understanding of how base-shale relief controls deformation, and the shape, size, and distribution of shale structures remain poorly understood. We here use 3D seismic reflection data from the Tarakan Basin, offshore Indonesia to investigate the temporal and spatial evolution of thin-skinned deformations of the Neogene sedimentary section. Our detailed seismic interpretation reveals long (≤ 74 km), concave- and convex-into-the-basin faults, dipping both basinward (eastwards) and locally landward (westwards), which detach downwards on a basal mobile shale (Middle Miocene). The base of the shale unit dips gently (< 17^{o}) seaward, although older (Paleogene), rift-related normal faults mean a local base-shale relief is present. Our analysis of isochron (thickness map) analysis shows that supra-shale normal faulting commenced in the Middle Miocene and was accompanied by the formation of hanging wall rollover folds and associated crestal grabens, with the subsequent along- and across strike migration of strain being related to the nucleation, lateral linkage, and reactivation of individual fault systems. Updip growth faulting was also accompanied by the downslope flow of mobile shale, margin-parallel and-perpendicular differential loading, and local contraction and mobile shale-upbuilding, resulting in the growth of large, margin-parallel shale anticlines further downdip. These faults and anticlines are locally overlain by tall (≤ 5 km) mud diapirs and volcanoes. We suggest that variations in the rate of sediment loading, mobile shale flow, fault growth, and gravitational failure above a seaward-dipping, but slightly rugose base-shale surface, controlled Neogene deformations in the Tarakan Basin. We also demonstrate how variations in the trend and dip of the base-shale surface influences the position, timing, and evolution of supra-shale faults and their associated depocenters along shale-rich, delta-fed clastic margins.

Keywords:

shale tectonic; base-shale relief; deltaic continental margin; gravity driven deformation; mobile shale flow

Highlight:

- Deformations in the Tarakan Basin, offshore Indonesia are characterized by basinward- and landward-dipping growth faulting, shale rollers and anticlines, and mud diapirs and volcanoes
- Growth faults grew by tip propagation and segment linkage, with late-stage tip retreat and reactivation also occurring
- The structural style and kinematics record spatial variations in the rate of sediment loading, mobile shale flow, fault growth, and gravitational failure above a rugose base-shale surface
- Variations in the trend and dip of the base-shale surface controls the position, timing, and evolution of supra-shale faults and their associated depocenters

1. **Introduction**

Shale-rich, deltaic continental margins may be characterized by thin-skinned, gravity-driven deformation above an unconsolidated, overpressured, buried shale (e.g. Damuth, 1994; Morley and Guerin., 1996; Cohen and McClay, 1996; Briggs et al., 2006, Santos Betancor and Soto, 2012; Zhang et al., 2021). However, difficulties with seismically imaging remobilized shale bodies mean that we have a poor understanding of the shape and size of these features, and the mechanisms (e.g., brittle vs. ductile) driving deformation (see Hudec and Soto, 2021). For example, previous 2D seismic-based studies identify chaotic seismic facies interpreted to reflect thick, mobile shale and overlying, shale-detached listric normal faults (e.g. Damuth, 1994; Morley and Guerin., 1996; Cohen and McClay, 1996). However, in higher quality data imaging the similar area, a structurally much simpler, fault-related horst may be interpreted, with a large shale body being absent (Van Rensbergen and Morley, 2000). This illustrates how improvements in subsurface imaging can provide a better understanding of the structural style and kinematic evolution of shale tectonics along deltaic continental margins.

In the proximal domain of deltaic continental margins, thin-skinned deformation is typically characterized by basinward- and landward-dipping listric growth faults and mud diapirs (e.g. Damuth, 1994; Van Rensbergen et al., 1999; Sapin et al., 2012; Ahmed et al., 2022). Extensional deformation of the supra-shale overburden and the rise of diapiric shale are controlled by rapid progradation of sedimentary wedges and gravitational gliding (e.g. Evamy et al., 1978; Cohen and McClay, 1996; Morley, 2003). The ultimate structural style and evolution are influenced by differential compaction of the progradational succession (e.g. Van Rensbergen and Morley, 2000), the presence of pre-existing shale structures (e.g. Sapin et al., 2012; Fazlikhani and Back, 2015), temporal and spatial variations in sediment accummulations rates (e.g. Chima et al., 2022), the existence of fluid expulsion structures (Back and Morley, 2016), the occurrence of a base-shale relief (Chima et al., 2022), the deep flow of mobile shale under either brittle or ductile conditions (e.g. Cohen and McClay, 1996; Soto et al., 2021a), and the growth history of supra-shale faults (e.g. Fazlikhani and Back, 2012). Most of studies listed above provide only two-dimensional treatments of shale tectonics and only very few have inspected their three-dimensional evolution (Fazlikhani and Back., 2012, 2015; Ahmed et al., 2022).

The Tarakan Basin, offshore Indonesia is an example of a deltaic continental margin containing thick, mobile shale (Fig. 1). The basin is separated from the onshore region by thick-skinned normal faults (e.g. Hidayati et al., 2007). The offshore area is characterized by shale-detached (i.e., thin-skinned), NE-SW-striking, basinward- and landward-dipping extensional (e.g. Heriyanto et al., 1992, Lentini and Darman, 1996) or reverse (e.g. Biantoro et al., 1996; Maulin et al., 2021) growth faults, and several NW-trending folds, which have been traditionally called *isoclinal folds* (arches in Fig. 1; e.g. Wight et al., 1993). The kinematics and origin of the growth faults and folds are debated, falling into two end-member models: (i) a strike-slip faulting model (e.g. Wight et al., 1993; Lentini and Darman, 1996; Hidayati et al., 2007; Maulin et al., 2021); and (ii) a margin-uplift model (Sapiie et al., 2021). However, these previous studies use two-dimensional seismic reflection data that have relatively poor imaging of the deep basin, including the interval containing mobile Neogene shale. Thus, a study based on high-quality, preferably 3D seismic reflection data is needed to test these models and to underpin a detailed reconstruction of the structural style and evolution of the basin.

We here use high-quality, 3D seismic reflection datasets imaging the shelf-edge to upper-slope of the Tarakan Basin to answer the following two key questions: (i) what are the spatial and kinematic relationships between sub- and supra-shale deformations in the proximal domains of a shale-dominated delta; and (ii) how does the structural style and evolution of the Tarakan Basin during the Neogene relate to the broader tectonic and geodynamic setting of the region? We identify a deltaic system that prograded seaward into the Tarakan Basin across mobile shale and several N-to-NE-trending, base-shale highs. The delta, including its underlying mobile shale, is deformed by arrays of NW-SE-striking, shale-detached, basinward- and landward-dipping growth fault systems and shale structures (i.e. shale rollers, anticlines, mud diapirs, and mud volcanoes). Using seismic-stratigraphic and isochron analysis, we reconstruct six main stages in the post-Eocene structural evolution of the basin.

2. **Geological Setting**

The Tarakan Basin is located offshore NE Borneo Island, within Indonesia territory (Achmad and Samuel, 1984). The basin is located in a structurally complex zone of continental convergence involving subduction of Northern Sulawesi (e.g. Hall, 2013; 2019; Watkinson and Hall, 2017) (Fig. 1a). The western, yet still offshore part of the basin is thought to be separated from the eastern part of the onshore region by a large, thick-skinned normal fault (e.g. Hidayati et al., 2007). The Tarakan Basin stretches eastwards into Celebes Sea (Fig. 1a). To the north and south the basin bound by the Sampoerna and Mangkalihat strike-slip fault zones, respectively (e.g. Lentini and Darman, 1996).

Borneo Island and adjacent areas were subject to four main stages of Paleogene-to-early Neogene, lithospheric deformations (Fig. 2): (i) a clockwise rotation of ca. 12^o since 35 Ma (Cullen et al., 2012), and later, a counter-clockwise rotation of 50^o since 30 Ma (Fuller et al 1999); (ii) Eocene-Oligocene rifting involving the South China Sea (Cullen, 2014) and possibly the Celebes Sea (Pubellier and Morley, 2014); (iii) Oligocene-Early Miocene regional subsidence in NW (Cullen, 2014) and SE Borneo (Cullen, 2014; Pubellier and Morley, 2014), driven by sedimentary loading (Pubellier and Morley, 2014) and post-rift, lithosphere thermal cooling; and (iv) the Sabah orogeny in northern Borneo (Hutchison, 1996), which was created by collision of extended continental crust (e.g. North Palawan block) against the Sabah-Cagayan Arc (e.g. Hall., 2013). These tectonic events are recorded by the Eocene-Early Miocene sedimentary successions, more specifically several regional unconformities that span the South China sea and NW Borneo (e.g. Hutchison, 2005; Cullen, 2010, 2014; Madon et al., 2013).

Variations of the location and magnitude of lithospheric deformation and sedimentation occurred in the NE Borneo and adjacent areas during the Early Miocene. For example, the onset of the rapid accumulation of a turbidite-fed, smectite-rich clay (> 50% smectite, 25% illite, < 10% kaolinite, and < 5% chlorite) occurred at Early Miocene (ca. 18.5 Ma) in the Celebes Sea (Rangin and Silver, 1991; Silver and Rangin, 1991). In the Tarakan area, deltaic sedimentary deposition began up to 16 Ma (Achmad and Samuel, 1984), and onshore was associated with a marked increase in sediment accumulation rate (from 60 to 120 m/my) (Fig. 2; Hidayati et al., 2007). This period of basin development was important, given it was associated with deposition of the thick shale sequence now observed at the base of the Tarakan Basin (Achmad and Samuel, 1984). Sedimentation at this time was also coeval with Early Miocene collision of the Sulawesi and Sula blocks (Rangin and Silver, 1991; Silver and Rangin, 1991) and with three periods of global sea-level fall (Mi1; ca. 23 Ma, Mi2; ca. 16 Ma and Mi3; ca. 13.8 Ma) (Miller et al., 2020) (Fig. 2).

During the Middle-Late Miocene, the tectono-stratigraphic development of the Tarakan Basin and surrounding areas was controlled by lithosphere-scale (i.e., thick-skinned) and/or gravity-driven (i.e., thin-skinned) deformation. Listric growth faults formed (e.g. Wight et al., 1993; Lentini and Darman, 1996), detaching downward in Oligocene-Early Miocene (Maulin et al., 2021) or Early-Middle Miocene sequences (e.g. Hidayati et al., 2007; Putra et al., 2017; Sapiie et al., 2021). There are also deeper, rift-related normal faults affecting the basement- (Biantoro et al., 1996; Hidayati et al., 2007). Middle-Late Miocene deformation was coeval with a progressively increasing rate of sediment accumulations (from 120 to 330 m/my; Fig. 2). In northern Borneo, Neogene deformation was accompanied by subsidence in Central Basin of eastern Sabah, and the rapid accumulation of 15 km of sediments (Graves and Swauger., 1997; Hall, 2013). Subsidence was coeval with uplift in north-west Borneo, caused possibly by deep crustal flow in respond to sedimentary loading (Morley and Westway, 2006; Hall, 2013), or magmatic activity (Hall, 2013)

Since the Pliocene, the Tarakan Basin was subject to both folding and reverse faulting (Fig. 1a). Two alternative models haven been proposed to explain their origins: (i) wrenching along the Maratua and Sampoerna strike-slip faults (Wight et al., 1993; Lentini and Darman, 1996; Hidayati et al., 2007), or; (ii) distal uplift of the deeper faults (Sapiie et al., 2021), which resulted in inversion of formerly extensional listric normal faults, and the formation of NW-trending arches or folds (e.g. Wight et al., 1993; Lentini and Darman, 1996; Hidayati et al., 2007, Maulin et al., 2021). Regardless of their origin, formation of these structures occurred during the Pliocene-Recent (e.g. Lentini and Darman, 1996), a period characterised by a high sedimentation rate, which was as high as 800 m/my in shelfal areas (Fig. 2). In contrast, in the distal areas of the basin the sedimentation rate was <120 m/my, because much of the Plio-Pleistocene sediment supply was trapped on the shelf (Hidayati et al., 2007). A large eustatic sea-level fall (up to 120-130 m) occurred at 2.7 Ma (Pl in Fig. 2), which was followed by a progressive sea-level rise during the Holocene (Miller et al., 2020).

We focus on the shelf-edge to upper slope of the Tarakan Basin, where at least five different onshore-river systems supplied sediment to the offshore basin (Fig. 1). Wells in this proximal area reveal overpressure conditions within the Middle-Late Miocene sequences (Putra et al., 2017). According to previous studies, this offshore area contains a range of basinward- and landward-dipping extensional and/or inverted growth faults, and is situated at the southern tip of the Bunyu Arch (e.g. Wight et al., 1993; Lentini and Darman, 1996; Hidayati et al., 2007; Maulin et al., 2021; Sapiie et al., 2021).

3. **Datasets and Methods**

We focused on an area imaged by two 3-D Kirchhoff PSTM seismic reflection datasets (TBN-10 in the north and TBB-11 in the south; Table 1). These two datasets overlap by ~70 km^2, and have similar inline and cross line spacings of 25 m (see complete details of the seismic datasets in Table 1). Inlines (NE to N) and crosslines (NW to W) trend broadly normal and parallel to the bulk SE tectonic translation direction of the supra-shale cover, respectively. The seismic data are displayed with the Society of Exploration Geophysics (SEG) reverse polarity, whereby a downward increase and decrease in acoustic impedance are represented by a negative and positive reflection events, respectively.

Kirchhoff PSTM data has some disadvantages when attempting to image structurally and stratigraphically complex areas. For example, such data might contain fault shadows, and they may not image shale structures as well as other seismic reflection data types (e.g. Fagin, 1996; Elsley and Tieman, 2010; Soto et al., 2021b). Still, our PSTM data are of sufficient quality to distinguish the main shale and supra-shale structures (Tables 2-4; see also table S1-S2). These data are in time, thereby the height of shale structures, for example, are converted from two-way time (TWT) to kilometres using seismic velocity data (e.g. Johnson and Hansen, 1987), ranging from 3500 m/s at seismic horizon H1 to 1500 m/s at seabed (Table 2).

The seismic data were provided by TGS and are commercially sensitive. As such, we cannot provide the precise geographic location of the survey and related seismic profiles (although the dataset is located along a delta-fed part of NE Borneo; Fig. 1) or the specific locations of wells. NW-to-W-trending seismic profiles (i.e., crosslines) normal to the broadly north-easterly margin trend are displayed from north to south (Figs 3 and 4; see also appendix S1 for uninterpreted sections), and these accompanied by a margin-parallel profile trending north-east (Fig. 5). In the profiles, we also include an estimate of the dip of the base-shale surface (Figs 3-5). However, given that the sections are in time, dips are approximate and relative values.

We map seven key seismic horizons (H1, TMB, H2-7) by identifying distinctive reflections and their terminations (i.e. onlap, toplap, and unconformities; Mitchum et al., 1977) (Table 2). The critical top mobile shale (TMB) is not constrained by well data, given no wells drill that deeply in the Tarakan Basin. As such, we infer the presence of deep shale using the seismic-reflection criteria established by Elsley and Tieman (2010), Santos Betancor and Soto (2015), Soto et al. (2021b), and Hudec and Soto (2021) (Table 2). The ages of shallower, younger key horizons are established by integrating: (i) the regional tectonic events affecting Borneo since the Oligocene (Fig. 2); and (ii) published data from the Vanda-1 well (Netherwood and Wight, 1992; Wight et al., 1993). These show that H1 is Lower Miocene(?) (using age of regional unconformities identified in Borneo; i.e., SCSU of Cullen, 2010, 2014; EMU of Madon et al., 2013; DRU of Hutchison, 2005), whereas TMB and H2-H3 are early Middle-Upper Miocene(?). The age of younger seismic horizons (i.e., H4-H7; uppermost Miocene to Upper Pleistocene) are directly constrained by the Vanda-1 well.

We use our seismic interpretations to generate isochrone maps for the mobile shale and six overburden units. We realized that the base-mobile shale (H1) locally extends below the depth imaged by our seismic data (> 8.0 s TWT or 14 km in TBN-10; Table 1), resulting in an underestimation of mobile shale thickness in this area (Fig. 6). However, our data and derived maps clearly reveal the main shale structures present within the basin. Because of: (i) limitations of seismic velocity data to undertake a regionally consistent depth conversion (e.g. Johnson and Hansen, 1987; Francis, 2018); and (ii) our primary interest being in the relative rather than absolute changes of fault throw along strike (cf. Jackson et al., 2017), we also present the structure and isochrone map in time, rather than depth (ms TWT) (Figs 7 and 8).

4. Base-shale structural style

The base-mobile shale (H1) is defined by a continuous, weak, positive reflection, located immediately above the upper tips of supra-shale faults (Figs 3-5; Table 2). These faults are apparently planar, and dip steeply (~70°) basinward- and landward. The largest throw on these faults (≤ 1 s TWT or 1 km) is observed in the southwestern and southern area. The lower tips of these faults are below the depth imaged by these seismic data (Table 1).

The base-shale dips gently basinwards (1-17°); i.e., SE (Figs 3-5). This surface is broadly convex-upward, being characterized by local, N-to-NE-trending structural-highs (ca. 6-7.5 s TWT or 10-12 km) in the north and south, and a large structural low in the centre of the study area (Fig. 5). Base-shale relief is related to long (up to 27 km), NNE-SSW-striking normal faults. Most of these faults dip basinwards, although some segments, which are more abundant in the south, dip landward (Fig. 6a). Many of these faults are soft-linked by relay zones or hard-linked by shorter faults (cf. Peacock and Sanderson, 1991).

5. Shale Structures

The top-shale horizon is defined by a strong, negative reflection (TMB; Figs 3-5). Given that the presence of methane in undercompacted shales can produced a strong, negative reflection (e.g. Soto et al., 2021b), we speculate that the negative reflection observed here defines the contact between normally compacted shales and methane-rich (possibly undercompacted) mobile shales. The seismic sequence below the TMB reflection contains various diffractions and noise, although we locally observe continuous, weak-to-moderate amplitude reflections (label “x”; Fig. 5). Internal reflections similar to these have been observed in other regions, being interpreted either as a pre-existing, now-deformed stratigraphic fabrics, or a new deformation fabric formed by the flow of mobile shales under critical-state conditions (Soto et al., 2021b).

Mobile shale thickness map shows how this unit varies across the study area, being thickest in the centre and east, thinning northward and southward (Fig. 6b). The thickest mobile shale coincides with the structural low seen on the base mobile shale map in the centre of the area, whereas the thinner areas coincide with the base-mobile shale structural highs identified in the north and south (Fig. 6).

5.1 Shale rollers

These structures are defined by broadly symmetrical, triangular zones of mobile shale that have a pointed crest and which are flanked on one side by basinward-dipping, shale-detached normal faults (label SR; Table 3 and Figs 3-5). These structures are interpreted as shale rollers, with their geometry and relationship to normal faults suggesting they formed via reactive diapirism during thin-skinned extension (e.g. Morley and Guerin, 1996; Hudec and Soto, 2021). They are thus comparable to salt rollers formed in salt basins (e.g. Brun and Mauduit, 2009; Jackson and Hudec, 2017). Shale rollers are broadly distributed across the study area, typically trending N-to-NE, sub-parallel to the sub-shale normal faults (cf. Figs. 6b and 6a).

5.2 Shale anticlines

These structures are characterised by broadly symmetric, low-amplitude, long-wavelength anticlines, cored by mobile shales, and with a single, angular-to-rounded hinge line. These structures are up to 5.5 s TWT (8.8 km) tall (label SA; Fig. 4b) and they usually verge basinward (i.e. SE), with a sub-horizontal eastern limb and a more steeply-dipping western limb (≤ 55^{o} dip). These structures are restricted to the distal, eastern part of the study area, and their axes trend parallel to the shale rollers (i.e. N-NE; Fig. 6b).

5.3 Mud diapirs

Mud diapirs are defined by domains of very low reflectivity that locally contain some isolated, low-amplitude, chaotic reflections (label MD; Table 3 and Fig. 7b). The external boundaries of these structure are sub-vertical, crosscutting the adjacent, layered sequences that loss progressively their reflectivity towards the diapir (label “iii” in MD; Table 3). Mud diapirs occur as deep as the H2 reflection, with their shallower heads deforming sequences near the H4 reflection (label MD; Table 3 and Fig. 4b).

The seismic characteristics of the mud diapirs and the nature of their contacts with the host rock suggest the existence of pervasive fluid migration from the mobilized, overpressured muds that pierce the country sediments (e.g. Santos Betancor and Soto, 2015). The upper parts of some of the mud diapirs are characterised by a broad (up to 4.3 km wide), tear drop-shaped area of low reflectivity, which may contain isolated, internal reflections. These reflections may reflect remnant fragments of the host rock, imbedded within the ascending diapiric material, which itself is poorly reflective. The lower part of the mud diapirs is more difficult to identify, and is commonly defined by a narrow, sub-vertical domain with crosscutting reflections that connect with the crest of deeper, shale-cored anticlines (label "i" in MD; Table 3). The mud diapir seen in the distal area affects H2-H4, defining an elongated structure parallel to the underlaying shale anticlines (Fig. 7a-b).

5.4 Mud volcanoes

These structures are defined by conical mounds (e.g. Kopf, 2002) that are identified as deep as the H4 reflection structural level, and which can affect younger sequences up to the seabed (Fig. 3b; Table 3). The deeper domains of mud volcanoes, i.e., below H4, are accompanied by chaotic reflections that are seen above normal faults (F5; Fig. 3b). At the shallower level, near H7, they form elliptical edifices parallel to the deeper and adjacent normal faults (Fig. 3d). Given these observations, we suggest that mud volcanoes are formed by reactive diapirism, with mobile shale ascending along sub-seismic fractures developed above buried, seismically imaged normal faults (e.g. Hudec and Soto, 2021).

6. **Supra-shale Structures**

The supra-shale structural framework is characterized by two main types of structures (Table 4 and Figs 3-5). The first type is defined by major basinward (F1-F15)- and landward (C1-C3)-dipping listric faults that die-out downward into the mobile shales and which tip-out upward between H4 and the seabed. The basinward-dipping listric faults detach downward onto the flanks of shale rollers and are flanked by growth strata (Figs 3-5). These faults are common on the shelf margin-to-upper slope (Fig. 1b), suggesting they formed in response to overburden extension due to gravitational failure of the deltaic wedge within which they developed (e.g. Morley, 2003; Soto et al., 2010; Hudec and Soto, 2021), and/or extension driven by differential compaction and fluid expulsion (e.g. Van Rensbergen and Morley, 2000; Back and Morley, 2016). The landward-dipping listric faults in the south are, however, flanked by progressively younger growth strata basinward, suggesting they formed in response to sedimentary loading during delta progradation (Fig. 4) (e.g. Morley and Guerin, 1996; Ge et al., 1997; McClay et al., 2003; Sapin et al., 2012; Ahmed et al., 2022). The basinward- and landward-dipping listric faults are associated with synthetic normal faults that formed within the damage zones of the larger faults (e.g. McGrath and Davison, 1996), or that developed to accommodate locally high stresses occurring within relay zones between the major growth faults (Imber et al., 2003) (e.g. F7a-b; Fig. 3b or C1a-c and C3b-e; Fig. 4d).

The second type of supra-shale structure is defined by folds that are best-developed between H2 and H7, flanking the basinward- and landward-dipping listric normal faults (e.g., F1 in the north, and C1 and C3 in the south; Figs 3c and 4; Table 4). Given their relationship to shale-detached faults, we interpret them as hanging wall rollover folds (e.g. Dula, 1991; Imber et al., 2003; Brun and Mauduit, 2008). Above the fold crests we observe symmetrical grabens bounded by basinward- and landward-planar normal faults that either physically link with the deeper major faults with which the folds are associated, or detach downward within the overburden. For example, above F10, several basinward- and landward-dipping normal fault arrays form a symmetrical graben (Fig. 4d). Based on their location above the fold crest, we infer that these minor normal faults reflect crestal extension and faulting in response of outer-arc bending of strata (e.g. McClay, 1990; Dula, 1991; Morley, 2007; Erdi and Jackson, 2021).

Maps of H2-H7 illustrate the geometry of the various supra-shale normal faults (Fig. 7). Basinward-dipping normal faults occur across the study area, whereas the landward-dipping normal faults are restricted to the south. Some fault segments are separated by NNE- or SSW-dipping, largely undeformed relay zones, such as C3a-b in the southeast (Fig. 7). Many faults show broadly convex- and concave-landward geometries, such as F7-F8. Throw on the faults broadly decreases southward (Fig. 7).

7. Temporal evolution of supra-shale deformation

Having established the various shale structures and supra-shale structural styles, we now explore how these structures evolved in the shelf-edge to upper slope of the Tarakan Basin. We interpret the evolution based on observations from time-structure and isochrone maps (Figs 6-8; see also S2 for a larger version). As isochrone maps show temporal changes in sediment thickness, which we infer record changes in accommodation driven by the migration of structural deformation (Fig. 8a-f) (e.g. Wu et al., 2015; Erdi and Jackson, 2021).

7.1 Base-shale detachment (Eocene-Early Miocene?)

The base-mobile shale is an unconformity that detaches sub-shale faults from the overlying mobile shale unit. This surface is inferred to represent the 16-19 Ma unconformity that separates pre-rift and overlying post-rift successions in the South China and Sulu seas (e.g. Madon et al., 2013; Cullen, 2010, 2014). Given the geometries of the sub-shale faults (e.g., planar, basement-involved) are broadly consistent with the geometry of syn-rift faults in the region (e.g. Schlüter et al., 1996; Franke et al., 2008), we speculate that sub-shale extensional faults are related to (i) the Eocene-Early Miocene(?), thick-skinned (i.e., lithosphere-involved) extensional event; (ii) a c. 38^{o} of anticlockwise, post-Eocene rotation of the Borneo Island (Fuller et al., 1999; Cullen et al., 2012). Although a component of oblique-slip cannot be ruled out, we speculate that this faulting was dominated by dip-slip movements. The general seaward dip of the base-shale surface above these faults (Figs 3-4) likely reflects post-Miocene tectonic uplift of northern Borneo and its immediately offshore region (Fig. 2) (e.g. Hall., 2013).

7.2 Deposition and origin of the mobile shale unit (Early Miocene-early Middle Miocene?)

Based on the tectonic setting of the study area, we infer that the mobile shale unit is possibly Early-to early Middle Miocene (ca. 16-14.8 Ma). In the Celebes Sea, a turbidite-fed, smectite-rich shale unit was rapidly deposited around ca. 18 Ma (Rangin and Silver, 1991; Silver and Rangin, 1991). We extrapolate this interpretation to our study area, assuming that the thick, mobile shale unit was deposited at around the same time, above the aforementioned unconformity (Fig. 2).

Previous studies suggest that erosion of granodiorites in northern Sulawesi, which were uplifted during the collision between Sulawesi and the Sula Block during the Early to early Middle Miocene (15-18.8 Ma) (Bellon et al., 1991), were the source for the clay unit in the Celebes Sea (Rangin and Silver, 1991; Silver and Rangin, 1991). Northern Borneo may also have been a source area for the mobile shale unit in the Tarakan Basin based on the fact that: (i) the area underwent rapid uplift and erosion during the Early Miocene due to the Sabah Orogeny (e.g. Hall and Nichols, 2002; Hall, 2013); (ii) important fluvio-deltaic systems originated in north Borneo during that time (van Hattum, 2013); and (iii) rapid sediment accumulation rates characterise the Early-Middle Miocene depositional history of the basin (Hidayati et al., 2007) and Celebes Sea (Rangin and Silver, 1991; Silver and Rangin, 1991). We thus infer that the mobile shale unit in the Tarakan Basin was rapidly deposited during the Early-Middle Miocene by a clay-rich deltaic system.

Although we cannot conclusively resolve the exact nature of the processes mobilizing the shales, we speculate that the smectite-transformation, in combination with increasing shear stresses by normal faulting, could have jointly participate in creating overpressure conditions in this shaly unit (Soto et al., 2021a; Li et al., 2022). Rapid sedimentation of this clay unit likely lead to fluid entrapment, making it possible to achieve the critical-state conditions to permit essentially solid-state flow at relatively lower shear stresses.

7.3 Stratal unit 1 (early Middle Miocene?)

7.3.1 Description

SU1 was deposited immediately above the mobile shale and thickens across many of the supra-shale listric faults (F1, F8-F10, F12-15, C1a-c, C2, and C3c-d; Fig. 8a; Figs 3c, 4 and 5). We identify the following three key thickness patterns within SU1; (i) fault-controlled depocenters spanning the entire present-day trace length (e.g., F1, F10, F12-15 in the northwest and the southeast; Fig. 8a); (ii) fault-controlled depocenters only span a short portion of the present-day fault traces (e.g., F8b, F9, C1a-c, C2 and C3c-d; Fig. 8a); and (iii) fault-controlled depocenters flank onto normal fault traces that are physical contact with each other (F8a-b; Fig. 8a).

7.3.2 Interpretation

SU1 records 1 Myr time span of the ~16 Myr post-rift history, indicating listric fault arrays began to grow soon after the cessation of mobile shale deposition (Fig. 8g). Faults grew in two different ways, either by: (i) a synchronous increase in fault throw and length, with associated fault segment linkage (i.e. in cases where SU1 depocenters flank only a portion of the present-day fault trace length; e.g. F8b, F9, C1a-c, C2 and C3c-d) (e.g. Walsh and Watterson, 1988; Dawers et al., 1993; Cartwright et al., 1995; Mansfield and Cartwright, 1996) (Fig. 8a, g); or (ii) rapidly attaining their near-final lengths via lateral tip propagation (i.e. in the cases where SU1 depocenters span the present-day traces, e.g. F1, F10 and F12-15; e.g. Walsh et al., 2003).

More generally, nucleation of the supra-shale listric faults indicate establishment and progradation of one or several deltaic systems during the first 2.4 Myr post-rift history of the Tarakan Basin (c.f. Morley and Guerin, 1996; Sapin et al., 2012; Back and Morley, 2016) (Fig. 8g). This interpretation is consistent with an increasing sediment accumulation rate (i.e. from 60 to 120 m/my) in the onshore Tarakan Basin during Early-Middle Miocene (Hidayati et al., 2007), and with events of global sea-level falls at Mi1-Mi3 (Miller et al., 2020) (Fig. 2).

7.4 Stratal unit 2 (Middle-Upper Miocene?)

7.4.1 Description

Thickness patterns in the SU2 shows that fault-controlled depocenters broadly persisted adjacent to listric faults (F1, F7d-e, F8-F10, F12-15, C1a-c, C2, and C3c-d; Fig. 8b), although in detail we note that: (i) across fault-thickening now occurred along or at the lateral tips of the present day traces of the supra-shale listric faults (F3, F4a-b, F6, F7a, c, e, F8a-c, southern portion of F9, F11, F12 and C1b-c, and C3a-d; Fig. 4b-c and 8b); (ii) C3a-b cross-cut fault-related thickening on the upper tip of F12 (Fig. 4b-c); and (iii) the SU2 displays no thickness variation across the eastern portion of F1 (Fig. 8b).

Along the normal fault array in the southeast, SU2 displays thickness variations toward the axis of the mud diapir (MD; Fig. 8b). This unit is upturned, and is truncated by overlying units against the mud diapir flanks, while diverge reflections, a wedge-shape geometry and thicken away from the mud diapir (Fig. 4b). We also note that mud diapir-related thickness variations in SU2 appear inversely related to thickness variations associated with adjacent supra-shale faults (F12-F14) and the underlying mobile shale (Figs 4a-c and 8b). For example, across fault thickening toward the F12 occurs above an area where the underlying mobile shale is thin, whereas thinning of SU2 toward the diapir flank occurs where the underlying mobile shale is thick (Fig. 4b-c).

7.4.2 Interpretation

SU2 records thin-skinned, gravity-driven deformation during the subsequent ca. 5.6 Myr post-rift history of the Tarakan Basin, recording the complex growth and death of the supra-shale fault array. First, some preexisting normal faults continue to grow via tip propagation, relay breaching, and segment linkage (F1, F4a, F8, F9, F10, F12-15, C1a-b, C2 and C3c-d; Fig. 8h). (F7d-e and F8c-d), (F8a-c, C1a-d and C3a-d; Fig. 8h). This interpretation is supported by the observation that depocenters are distributed along the established faults (Fig. 8b). Second, new normal faults nucleated (F3, F4a-b, F6, F7a, c, F11, C3a; Fig. 8h). Finally, some fault segments became inactive (F1 and F12; Figs 4b-c and 8h). More specifically to the F12, this fault death due to grew of the C3a-b, which was relatively younger.

Normal fault growth during the Middle-Upper Miocene was coeval with the onset of shale anticlines growth in the southeast (SA; Figs 4b and 8b). The local truncation of SU2 by overlying unit along the fold limbs indicates that rates of fold-related uplift were even higher than the increasing and relatively high sediment accummulation rate (from 120 to 220 m/my; Fig. 2). Two possible mechanisms can explain the onset of folding at this time: (a) downslope gliding of the mobile shale producing distal contraction (e.g. Espurt et al., 2009; Soto et al., 2010; Ahmed et al., 2022); and (b) margin-parallel and perpendicular differential loading. The first mechanism is supported by the orientation of fold axes being parallel to the shale rollers and their associated normal faults (Figs 6b and 8b), indicating these distal contractional folds could be kinematically linked to up-dip extension (Fig. 8h). The second mechanism is supported by the inverse relationship between thickness patterns in the mobile shale and SU2. For example, SU2 thickens onto the F12-F14 where the top of mobile shale is structurally low (Fig. 4a-c), suggesting the existence of syn-depositional loading by normal faulting and shale-withdrawal that promoted mobile shale upbuilding at the core of the distal fold. This mechanism is also supported by fault-controlled depocenter on the SU2 are distributed relatively basinward to that observed in underlying stratal unit (Fig. 8b), suggesting a basinward migration of the prograding wedge. This basinward progradation of the wedge might produce differential margin-perpendicular sedimentary loading and a basinward migration and evacuation of the mobile shale creating horizontal (tectonic) compaction and fluid expulsion (e.g. Van Rensbergen and Morley, 2000; Back and Morley, 2016). Still, given that the base-shale structure has a larger depocenter in the central domain (Fig. 6a), differential parallel-margin sedimentary loading could also occur, resulting in an additional north-south (margin-parallel) flow of the mobile shales to fill that trough.

7.5 Stratal unit 3 (Upper?-uppermost Miocene)

7.5.1 Description

There are several important observations regarding SU3. First, SU3 thickens (by up to 2.25 s TWT or 3 km) across many of the major normal faults (F3-F4, F6, F7a, c-e, F8-F11 and C1a-d, C2, C3a, c-d; Fig. 8c). Second, SU3 broadly thickens towards and has a wedge-shaped geometry in the hanging wall of some listric faults that are located relatively basinward of those active during deposition of SU2 (F5, C3b, e and southern portion of C1c; Figs 3a-b, 4b-d, 5 and 8c). Third, SU3 also has a wedge-shaped geometry adjacent to and thickens towards the lateral tips of major faults (F2-F3 and northern portion of F7a, and F4a-b; Figs 3 and 8c). Fourth, SU3 thickens down relay zones developed between fault segments, such as observed along C3a-b in the southeast

(Fig. 8c). Fourth, in these domains SU3 shows subtle thickening across the entire length of crestal faults between the F10 and C1c-e, diverging, for example, toward the crestal faults situated above F10 and C1c-e (Fig. 4b-d). Fifth, lower part of SU3 thickens toward C1a-b, while the upper part of the unit and fault are cross-cut by the rotated crestal faults (Fig. 4d). Finally, although SU3 generally thickens across them, this unit shows a constant thickness and a tabular geometry across the lateral tips of some of the major basinward-dipping normal faults situated in the western area (F7c-d, C2, and C3a, d; Fig. 8c).

SU3 thins and is upturned towards the mud diapir flanks (MD; Fig. 8c). The top of SU3 is also eroded at the base of the overlying unit, SU4 (MD; Fig. 4b).

7.5.2 Interpretation

Using thickness patterns in and the overall seismic-stratigraphic architecture of SU3, we can reconstruct the tectonic processes during the subsequent ca. 1.9 Myr post-rift history of the basin. Four key tectonic processes related to supra-shale extensional faulting occurred at this time. First, the existing normal faults continued to grow (F2-F4, F6-F7, F8a-b, F9-F11, C1c-d, Fig. 8i) via tip propagation (C1c and F7) and locally, hard-linkage by relay-breaching (F2, F7, and F4a, b). As a result, both basinward- and landward-dipping normal faults have a final convex-towards-the-basin geometry (Fig. 8b-c). Second, formation of relay zone along C3a-b, e and nucleation of F5 (Fig. 8i). Third, crestal faults above rollover anticline nucleated in response to clockwise tilting of the C1c-e and F10 (Fig. 8i). We interpret that the crestal faults were formed similarly to crestal faults, having originated above the hanging wall rollover associated with listric supra-shale faults (e.g. Dula, 1991; McClay, 1990). Fourth, during this time, some established faults like F3, F7d-e, F13, F15, C1a-b, C2 and C3c-d underwent tip retreat or became inactive (Fig. 8i). More specifically, some faults are inactive due to: (i) cross-cutting by listric and crestal fault formations that are relatively younger (C1a-b and F13-15; Fig. 4a, d), or; (ii) strain migration toward an incipient new footwall breaching of C3b,e within a large soft-linked relay zone (C3a-e; Figs 4 and 7) (c.f. Walsh et al., 1999; Imber et al., 2003).

These processes of fault growth and decay result in complex structural styles and evolution during the Upper?-uppermost Miocene in the shelf-edge of Tarakan Basin. We also noted a difference in the style of growth faulting during the Upper?-uppermost Miocene, showing by a relatively simple series of basinward-dipping listric faults in the north, and a complex series of roller folds, basinward- and landward-dipping listric with associated crestal faults in the south (Fig. 8i).

Two processes could explain these along-strike differences in structural style and kinematics. First, the process of horizontal compaction and fluid expulsion may have migrated northward along the margin, accompanied by the northwards flow of mobile shales. This interpretation is supported by: (i) base-shale relief being deeper in the north; (ii) mobile shale being thicker in the north; and (iii) mud volcanoes being preferentially developed in the north, coinciding with the domain of thicker mobile shale (Figs 3b and 6). This interpretation seems to perhaps conflict with the interpretation of higher sediment accumulation rates in the north (240-330 m/my) than the south (120-240 m/my) (Fig. 2). In our view, the existence of higher sediment accumulation rates, rather than being a barrier to fluid and shale flow, induced the ductile flow of mobile shales from the central depocenter toward the north.

The second explanation is that the difference in overburden structural styles reflects along-strike differences in the timing and magnitude of tilting of the mobile shales and their basal surface. Seaward tilting of this surface is up to 17° in the north, whereas it is lower in the south (4-7°) (cf. Figs 3 and 4). This interpretation is consistent, for example, with the study of Wu et al. (2015) and with the results from several physical models of shale-rich deltas (e.g. Mourgues et al., 2009), which suggest that landward-dipping listric fault systems are better developed when the dip of the mobile shales and their basal surface is relatively gentle.

Besides the overburden deformations, the SU3 growth strata also record a deformation linked to the mobilization of the shale unit in the southeast (MD; Figs 4b and 8c). We infer that the growth of the anticline in the southeast during the deposition of SU3 led to crestal faulting, with these structures providing pathways for the ascent of mobile shale, resulting in the emplacement of mud diapir (c.f. Bonini and Mazzarini, 2010; Bonini, 2012). This interpretation explains the spatial relationship between the fold hinge and the diapirs, as well as the basinward and the northward (i.e., along-strike) flow of mobile shale.

7.6 Stratal unit 4 (Uppermost Miocene-Pliocene)

7.6.1 Description

SU4 thickens across F2-F11, C1c-d, C3a-b,e and down the associated relay zones (Fig. 8d). Although this unit shows local thickening in the hanging wall of normal faults, we also observe: (i) a constant thickness along the trace of many shale-detached (F7c, southern tips of F3, F8a-b, F7d, e, and F9) and crestal normal faults (along C1c-d; Fig. 8d); and, (ii) thinning onto footwall of C3a-b due to erosion at the base of the overlying unit, SU5 (E2; Fig. 4). The area of erosion trends sub-parallel to these faults (Fig. 8d).

SU4 varies in thickness adjacent to mud diapirs and volcanoes in the southeast and the north of the study area (MD and MV; Fig. 8d). In the southeast, this unit is upturned towards and thins above the diapir crest (MD; Fig. 4b and Table 3). However, in the north, the upper interval of this unit shows chaotic reflections above the F5 (Fig. 3b and Table 3).

7.6.2 Interpretation

The seismic-stratigraphic patterns in SU4 are used to reconstruct the tectonic processes during the subsequent ca. 3.7 Myr post-rift history of the basin. The processes are illustrated by the on-going growth of pre-existing listric faults of F2, F4-F8, F11 and C1c-d, and the relay zone of C3a-b, e (Fig. 8j). More specifically to the F4a-b and F11, they grew via lengthening, and the later subsequently being followed by a hard-linkage(Fig. 8d). Fault growth and hanging wall tilting was also associated with the erosion of previously deposited strata (e.g. C3a-b; Fig. 8d, j). We interpret that faults grew in response to continued progradation of the sedimentary wedge and related differential compaction of and fluid expulsion from the mobile shales (e.g. Van Rensbergen and Morley, 2000), with the latter process being particularly important in the south (i.e. F8c-d, F9-F10; Fig. 8j). Some faults also underwent tip retreat and/or became inactive (e.g. F3, F7d-e, F8a-b, F9, C1e, F9 and C1c-d; Fig. 8j).

Variations in mobile shale-related deformations continued to occur along the margin during Upper Miocene-Pliocene, being illustrated by mud diapirism that was ongoing growth and initiation in the southeast and north respectively (MD and MV; Fig. 8j).

7.7 Stratal unit 5 (Pliocene-Pleistocene)

7.7.1. Description

SU5 is broadly tabular, thickening locally towards F2 and F8-F10, and showing a wedge-shaped geometry toward the hanging walls of F3-F7, F11, C1d-e, and C3a-b (Figs 3-5). There are further local variations in thickness compared to what we observe in underlying strata. First, SU5 displays subtle thickening towards and along C1e and fault-related crestal grabens along C1c-d (Figs 4b-d and 8e). Second, this unit has a constant thickness across the southern tip of F3 and along F4a-b (Fig. 8e). Third, SU5 varies in thickness around F4, F9, F11, and along the crestal faults C1c-e (Fig. 8e). These variations appear to be related to erosion of the top of the unit, being located in the hanging wall of listric and crestal normal faults, and at the base of SU6 (label E3 and E4; Figs 3a-b and 4).

SU5 also varies in thickness around mud diapirs and volcanoes (Fig. 8e). In the southeast, the lower part of this unit thins and onlaps above SU4 toward the crest of a mud diapir, whereas the upper part of the unit thickens and wedges eastward (Fig. 4b). In the north, however, SU5 show continuous mound shape geometries above the F5 (label MV; Fig. 3b).

7.7.2. Interpretation

The geometry of SU5 records the tectonic processes during the subsequent ca. 2.58 Myr post-rift history of the basin . Overburden extension continued as shown by the continued growth of F11, C1c-d and C3a, e, and the reactivation of some crestal normal faults above C1c-d (Fig. 8k). More specifically to the reactivation of the crestal faults that were formerly inactive during Pliocene, we infer that this fault reactivation was due to another pulse of strata bending in response to clockwise hanging wall rotation of the C1c-d fault (Figs 4b-d and 8e).

During the Pliocene-Pleistocene, the mud diapir in the south were buried due to either it stopped grow or a larger sedimentation rate with respect to the rate of mud ascent (Fig. 8k). In the north, however, a mud volcanism occurred (MV; Fig. 3b).

7.8 Stratal unit 6 (Pleistocene-Holocene)

7.8.1 Description

SU6 thickens across (F2, F4-F7, F9, C1, and C3; Fig. 8f) and/or is wedge-shaped in and diverges towards the hanging walls of (C1c and C3a-b; Fig. 4) supra-shale normal faults. In contrast, it is broadly tabular adjacent to F2, F4-F7, and F9 (Figs 3a-b and 4b-c). The unit, however, thins toward and onlap onto the mud volcano (Figs 3b and 8f).

7.8.2 Interpretation

SU6 record the latest tectonic activity in the margin, during the last 0.012 Myr. Tip retreat of many supra-shale faults occurred during this time (Fig. 8l), with many faults dying-out (Figs 3-5). However, some faults remained active (i.e. F2, F4a, F5-6, F7b and F9a-b; Fig. 8f, l), coincident with and possibly driven by, an increase in the rate of sediment accumulation (from 180 to 820 m/my) (Fig. 2). The mud volcano in the north, however, continued to grow via shale fed along fractures (MV; Fig. 8l).

8. **Discussion**

8.1 Structural styles in the Tarakan Basin

Previous 2D seismic-based studies show that NW-trending arches (e.g. Wight et al., 1993; Lentini and Darman, 1996), NE-SW-striking rollover folds, and listric (e.g. Wight et al., 1992; Biantoro et al., 1996), thick-skinned normal (Hidayati et al., 2007), reverse, inverse normal (e.g. Wight et al., 1993), and/or NW-SE-striking strike-slip faults (e.g. Wight et al., 1992; Lentini and Darman, 1996; Sapiie et al., 2021) are all developed in the offshore Tarakan Basin (Fig. 1). All previous studies agree that Miocene gravity-driven failure led to listric faulting and related folding (e.g. Van Bemmelen, 1949; Hidayati et al., 2007; Sapiie et al., 2021). However, the post-Pliocene kinematic development of the isoclinal fold and inversion normal faults mentioned above is debated, with two-end member models proposed: (i) wrenching or transform faulting (Wight et al., 1993; Lentini and Darman, 1996; Hidayati et al., 2007); or (ii) the uplift of pre-existing rift-related topography (Sapiie et al., 2021; Ahmed et al., 2022). These studies have, however, some important limitations. For example, (i) they lack a comprehensive reconstruction of the structures in map-view, characterizing key structures like fault tip lines and branch lines, sedimentary facies boundaries, and fold axes (e.g. Sylvester, 1988; Erdi and Jackson, 2022), which collectively make it possible to evaluate fault and fold geometry and kinematics (e.g. Harding, 1990); and (ii) widely spaced (> 62.5 m) 2D seismic data mean it is hard to determine the geometry and evolution of inherently 3D structures such as segmented normal faults and geometrically complex shale structures (e.g. Tearpock and Bischke, 2002; Groshong, 2006; Ze and Alves, 2019).

Our detailed 3D seismic interpretation constrains the structural style and distribution of shale and supra-shale structures, showing many occur above NE-trending base-shale relief that inferably has a concave-basinward geometry, and which are superimposed on a generally seaward-dipping surface (Fig. 9). Above this surface, the basal mobile shale unit shows extensional (e.g. shale rollers and shale-detached normal faults) and contractional (anticlines) structures. We also interpret that the mobile shale flowed upward, forming mud diapirs and volcanoes that pierced a few kilometres of overburden strata and that were active until recently (i.e. they are locally expressed at the seabed). Supra-shale deformations consist of concave- and convex-basinward arrays of extensional listric growth faults, and related hanging wall rollover folds and outer-arc bending-related crestal faults.

In our dataset we also observe the southern tip of the Bunyu Arch; this is a major structure previously described as a series of NW-trending isoclinal folds (Figs 1 and 7; Wight et al., 1993; Lentini and Darman, 1996). In our view, rather than comprising several isoclinal folds, this structure is represented by several NE-trending rollover folds associated with large, shale-detached listric growth faults (Figs 7 and 8). Thus, in contrast to the previous interpretations, we suggest that other similar isoclinal folds or arches in the Tarakan Basin are *en echelon*, basement-detached rollover folds (Fig. 1).

In summary, we propose that the Neogene structural style of the Tarakan Basin reflects (Fig. 9): (i) variations in sediment accumulation rates and the progradation of deltaic sedimentary wedges from northeastern Borneo, (ii) the dominantly seaward flow of the basal shale unit (lowermost Middle Miocene) to induce inflation of mobile shale unit in the distal domain, possibly with a contribution of margin-parallel flow to generate the large, central depocenter and drive mud diapirism and volcanism in the north (Fig. 6b), (iii) the growth and linkage of the supra-shale extensional fault systems (Fig. 8), and (iv) associated gravitational failure of the Neogene sedimentary wedge, induced by irregular seaward tilting of the entire margin (Fig. 6a), driven by plate-scale uplift of Borneo (e.g. Hall, 2013).

8.2 Deltaic growth faulting: geometry, timing, and tectonic significance

Previous studies demonstrate that the geometry, distribution, and kinematics of growth faulting in shale-rich deltas are controlled by the interaction between gravity gliding downslope associated with margin uplift (e.g. Garfunkel, 1984; Gawthorpe et al., 1994) and sediment loading during delta progradation (e.g. Evamy, 1978; Cohen and McClay, 1996; McClay et al., 2003) above an overpressured shale (e.g. Mandl and Crans, 1981; Mourgues et al., 2009; Lacoste et al, 2012; Fernández-Ibañez and Soto, 2017) and/or differential compaction (e.g. Van Rensbergen and Morley, 2000. Still, fault growth and linkage (e.g. Fazlikhani and Back., 2012), base-shale slope angle (e.g. Wu et al, 2015; Lacoste et al., 2012), and/or differential compaction and associated fluid expulsion (e.g. Van Rensbergen and Morley, 2000; Back and Morley, 2016) can also contribute to development of the growth faulting. Fault-related strain can migrate basinward as the causal sedimentary wedge progrades (e.g. Evamy, 1978; Cohen and McClay, 1996; McClay et al., 2003; Mourgues, 2009; Ahmed et al., 2022). Faulting can also migrate landward migration, through lateral fault-linkage (e.g. Fazlikhani and Back, 2012; Imber et al., 2003) accompanying the general downslope gliding of the sedimentary wedge due to the seaward tilting of the margin (e.g. Lacoste et al., 2012). Variations in the dip of the seaward tilted base-shale also controls the locus of faulting and the dip direction of the growth faults. This is because an increase in the dip of base of shales tends to produce basinward-dipping growth faults, whereas a relatively gently-dipping shale base usually promotes the formation of landward-dipping growth faults (e.g. Wu et al., 2015). Sediment loading can also promote the local escape of fluids and mud, forming the intrusion (e.g. diapirs) and extrusion (e.g. volcanoes) of shale (e.g. Van Rensbergen and Morley, 2000; Back and Morley, 2016).

Our study shows that the distribution of landward- and basinward-dipping deltaic growth faulting varies in time and space along the proximal, shelf-edge region of the Tarakan Basin. The basinward-dipping faults are broadly developed above areas where the base-shale dips more steeply dipping (≤ 17°) basinward, whereas the landward-dipping faults are preferentially developed above segments of the surface defined by a relatively gentle dip (4-7°) steps (Fig. 9). The locus of basinward growth faulting is consistent with the study of Wu et al. (2015), given they show how domains with a gentle dip of the shale base tend to nucleate landward-dipping growth faults. Here we also demonstrate that growth faulting migrates landward and basinward during the Neogene, possibly in response to varying sedimentation rates of the delta systems prograding from the eastern margin of Borneo (Fig. 9). Landward migration of extensional faulting occurred above relatively steep-dipping base-shale relief in the north, whereas basinward migration occurred above the relatively gentle-dipping base-shale relief in the south. These inferences are also in agreement with (i) the lateral propagation and linkage of basinward-dipping listric faults in the north, and basinward- and landward-dipping listric faults in the south, and; uplift in north Borneo since Miocene (e.g. Hall, 2013).

9. **Conclusions**

We conducted a seismic-stratigraphic analysis of 3D seismic reflection data from the shelf-edge to upper slope of Tarakan Basin, offshore Indonesia to unravel the lateral variability in the structural style, distribution, and kinematics of thin-skinned, shale-related deformation. We showed that the Tarakan delta system, including its underlying basal mobile shale, is deformed by a range of shale structures (i.e. shale anticlines, mud diapir and volcanoes), and basinward-and landward-dipping growth faults located above and trending parallel to NE-trending base-shale highs developed above an older rift. Using isochrone (thickness) maps we identify four main tectono-stratigraphic stages: (i) Eocene-early Middle Miocene? - continental rifting and deposition of the mobile shale unit; (ii) Middle-Upper Miocene? - fault nucleation, growth, and linkage in the proximal domain, and formation of a shale-cored anticline in a more distal area; (iii) Upper Miocene-Pliocene - lateral propagation and eventual retreat of the extensional faults, and mud diapirism; (iv) Pleistocene-Holocene – extensional faults reactivation, decay and death, and mud volcanism. Our study suggests the temporal and spatial evolution of Neogene deformations in the shelf-edge to upper slope region of the Tarakan Basin reflects the interaction between variations in sediment accumulation rate and the progradation of deltaic sedimentary wedges, mobile shale flows, the growth and linkage of extensional fault, and the associated gravitational failure of the shale-rich deltaic above base-shale relief. More specifically our study further highlights the key relationship between the direction of strain migration and the geometry of the basal detachment in gravity-driven deformation systems, with landward-directed migration occurring above regions defined by steeply seaward-dipping relief, and basinward-directed above relatively gentle basal relief. These learnings can provide insights into the structural styles and kinematics observed on other shale-rich margins, such as that characterizing the Mahakam and Niger deltas, and the Ceduna sub-basin, offshore South Australia.

Acknowledgment

This study represents the PhD research of the first author, being sponsored by the Indonesia Endowment Fund for Education (LPDP) (Grant/Award Number: 201712220212151). This research is administratively supported by formerly Research Center for Geotechnology, Indonesian Institute of Science (LIPI) (now National Research and Innovation Agency, - BRIN). The first author wishes to thank Robert Hall, Perdana Rakhmana Putra, Danny Hilman Natawidjaya, Maruf Mukti, and Mudrik Rahmawan Daryono for discussions during this study. A big thank you to TGS for providing access to the high-quality 3D seismic dataset and for allowing publication of the results of this study. The authors also acknowledge Schlumberger for providing Petrel software to Imperial College London. JIS acknowledges the financial support of the Applied Geodynamics Laboratory (AGL) Industrial Associates program, comprising the following companies: Anadarko, Aramco Services, BHP Billiton, BP, CGG, Chevron, Condor, Ecopetrol, EMGS, ENI, ExxonMobil, Hess, Ion-GXT, Midland Valley, Murphy, Nexen USA, Noble, Petrobras, Petronas, PGS, Repsol, Rockfield, Shell, Spectrum, Equinor, Stone Energy, TGS, Total, WesternGeco, and Woodside (http://www.beg.utexas.edu/agl/sponsors). Publication authorized by the Director, Bureau of Economic Geology, The University of Texas at Austin.

Table Captions

Table 1: Description of seismic dataset used in our study in Tarakan Basin, Offshore Indonesia.

Table 2: Characterization, seismic velocity and tectonic significance of the interpreted seismic horizons of the Neogene section of the Tarakan Basin, offshore Indonesia, as seen in the shelf-edge and upper slope of the basin.

Table 3: Summary of the diagnostic seismic characteristics of the shale structures identified between the shelf-edge and upper slope of Tarakan Basin, offshore Indonesia. See also Table S1 in Appendix for a larger version of this table. Seismic data courtesy of TGS.

Table 4: Summary of principal characteristics of the supra-shale faults as they are seen in the area between the shelf-edge and upper slope of Tarakan Basin, offshore Indonesia. See also Table S2 in Appendix for a larger version of this table. Seismic data courtesy of TGS.

Figure captions

Figure 1: Regional tectonic map and section of Tarakan Basin. Although precise location cannot be released due to confidentiality, the study is around the shelf-edge to upper slope of the extensional domain of this basin. (a) Simplified regional structural map illustrating key tectonic features in the north-east Borneo, consisting of Tarakan (TA), Bunyu (BA), Ahus (AA) and Sebatik (SA) arches, major regional normal fault (MRNF), like the Sampurna (SFZ) and Maratua (MFZ) fault zones. Map modified from Wight et al. (1993), Lentini and Darman (1996), Moss et al. (1998), Hidayati et al. (2007), and Balaguru and Hall (2009). Well locations are taken from Wight et al. (1993), Corelab (2007), and Chakhmakhchev and Rushworth (2010). Base map is derived from GEBCO (2020). (b) Regional cross section (modified from Hidayati et al., 2007).

Figure 2: Regional tectono-stratigraphic framework chart of Paleogene to Quarternary (Q) in north-west and north-east Borneo (modified and simplified with information from Hall, 2012, 2013, 2019). Formation in this chart can be simplify into syn-rift, mobile shale and supra mobile shale unit. The syn-rift and mobile shale unit are separated by a regional South China Sea (SCSU) or Early Miocene (EMU) unconformity that have Early-Middle Miocene age (Cullen,

2010, 2014; Madon et al., 2014). This chart is compared with the global eustatic sea level curve that shows global sea level drop (Mi1-2 and PI) and rise (Mi3) (Miller et al., 2020), and sedimentary rates for the Tarakan Basin derived from well data (modified from Hidayati et al., 2007). It is shown our interpretative seismic horizons and units differentiated in the Neogene sequence of the shelf-edge of Tarakan Basin, offshore Indonesia. Well locations and source area of sediment budget are shown in Fig. 1.

Figure 3: Selected seismic profiles showing the configuration of the Tarakan Basin in a direction parallel to the regional dip (approximately 1-17°) of the mobile shale base, which is parallel to bulk translation direction of the supra-shale cover. It is also illustrated the style of growth faulting and how it varies laterally in the northern part of the study area. Due to confidentiality, the exact position of the NW-SE seismic sections (a–c) is omitted here. Uninterpreted version of the three seismic profiles are shown in Appendix S1. Seismic data courtesy of TGS.

Figure 4: Margin parallel seismic sections illustrating the styles of growth fault systems in the southern part of the study area. The W-E orientation of the four seismic lines (a–d) is sub-perpendicular to the regional dip (approximately 4-5°) of the base of mobile shale, and to the bulk translation direction of the supra-shale cover. Notes of “x” show layering of seismic facies that may reflect relict or new deformation intra-fabrics within mobile shales. Due to confidentiality, the exact position of the seismic sections (a–c) is omitted here. Uninterpreted version of the four seismic profile is shown in Appendix S1. Seismic data courtesy of TGS.

Figure 5: Composite, SW-NE margin-parallel seismic section illustrating shale and supra-shale structural styles. This orientation is normal to the regional dip of the base of mobile shale and to the bulk translation direction of the sedimentary cover. This section also shows the present relationship of the basin with the sub-shale sequences, which are deformed by high-angle normal faults related to the Paleogene continental rifting (Fig. 2). Notes of “x” show layering of seismic facies that may reflect relict or new deformation intra-fabrics within mobile shales. Uninterpreted version of the seismic profile is shown in Appendix S1. Seismic data courtesy of TGS.

Figure 6: Base-shale surface and mobile shale isochrone maps (interval contour of 250 ms). (a) Base-shale structural map, illustrating spatial geometry of base-shale relief that probably reflects the inherited rift topography. This map also records the geometry and distribution of N-S sub-shale faults. (b) Mobile shale isochrone map (in s TWT), illustrating morphology and distribution of shale in the basin. To compare, it is included the distribution and type of structures affecting the top of mobile shale (TMB), including shale roller and anticline (see Table 3 for description of these shale structures).

Figure 7: Overburden structural maps of the main supra-shale seismic reflections (interval contour of 250 ms): (a) H2 - Middle Miocene, (b) H4 - Uppermost Miocene, and (c) H7 - Upper Pleistocene (Fig. 2). These maps contain information regarding structures affecting the supra-shale sequences, as basinward and landward normal faults, but also mobile shale structures like mud diapirs, and mud volcanoes. Table 3 and 4 contain a detailed description of the seismic expression and their differentiating characteristics of these structures.

Figure 8: Overburden isochrone maps of all the supra-shale seismic units differentiated in this study (interval contour of 250 ms) (Fig. 2): (a) SU1 - Middle Miocene; (b) SU2 - Middle-Upper Miocene; (c) SU3 - Upper-Uppermost Miocene; (d) SU4 - Uppermost Miocene-Pliocene; (e) SU5 - Pliocene-Pleistocene; (f) SU6 - Pleistocene-Holocene, accompanied in (g-l) by their tectonic interpretation. These interpretative sketches illustrate the Neogene tectonic evolution of the Tarakan Basin in the study area, detailing the activity of shale and supra-shale structures at every particular time. See also Appendix of S2 for a larger version of overburden isochrone and their interpretative sketches.

Figure 9: Regional map summarizing the main findings of our study, and general schematizing the structural elements controlling the Neogene evolution of the offshore area of Tarakan Basin, north-east Borneo, like the distribution and role played in the margin by supra-shale growth faulting (either with basinward and landward normal faults), the flow pattern inferred for mobile shales, the distal shale inflation and contraction, as well as the occurrence of steps in the base of mobile shales, induced by sub-shale faults, which are possibly inherited from the Paleogene rifting.

Data Availability Statement

The seismic data supporting the findings of this study are available from TGS. However, restrictions apply to the availability of these data, which were used under license for this study.

References

Achmad, Z., & Samuel, L. (1984). *Stratigraphy and depositional cycles in the N.E. Kalimantan Basin.* Paper presented at the Indonesian Petroleum Association, 13th Annual Convention and Exhibition Jakarta, Indonesia.

Ahmed, B., McClay, K., Scarselli, N., & Bilal, A. (2022). New insights on the gravity-driven deformation of late Albian – early Turonian stacked delta collapse systems in the Ceduna sub-basin, Bight Basin, southern margin of Australia. *Tectonophysics*, 229184. https://doi.org/10.1016/j.tecto.2021.229184

Back, S., & Morley, C. K. (2016). Growth faults above shale – Seismic-scale outcrop analogues from the Makran foreland, SW Pakistan. *Marine and Petroleum Geology, 70*, 144-162. https://doi.org/10.1016/j.marpetgeo.2015.11.008

Balaguru, A., & Hall, R. (2009). *Tectonic Evolution and Sedimentation of Sabah, North Borneo, Malaysia*. Paper presented at the AAPG International and Exhibition Cape Town, South Africa

Bellon, H., and Rangin, C. (1991). Geochemistry and isotopic dating of Cenozoic volcanic arc sequences around the Celebes and Sulu seas. *In:* Silver, E. A., Rangin, C., von Breymann, M. T., et al. (Eds.), *Proc. ODP, Sci. Results,* 124: College Station, TX (Ocean Drilling Program), 321–338. https://doi.org/10.2973/odp.proc.sr.124.163.1991

Biantoro, E., Kusuma, M. I., & Rotinsulu, L. F. (1996). *Tarakan sub-basin growth faults, North-East Kalimantan: Their roles in hydrocarbon entrapment*. Paper presented at the Indonesian Petroleum Association, 21st Annual Convention and Exhibition, Jakarta, Indonesia.

Bonini, M. (2012). Mud volcanoes: Indicators of stress orientation and tectonic controls. *Earth-Science Reviews, 115*(3), 121-152. https://doi.org/10.1016/j.earscirev.2012.09.002

Bonini, M., & Mazzarini, F. (2010). Mud volcanoes as potential indicators of regional stress and pressurized layer depth. *Tectonophysics, 494*(1), 32-47. https://doi.org/10.1016/j.tecto.2010.08.006

Briggs, S. E., Davies, R. J., Cartwright, J. A., & Morgan, R. (2006). Multiple detachment levels and their control on fold styles in the compressional domain of the deepwater west Niger Delta. *Basin Research, 18*(4), 435-450. https://doi.org/10.1111/j.1365-2117.2006.00300.x

Brun, J.-P., & Mauduit, T. P. O. (2009). Salt rollers: Structure and kinematics from analogue modelling. *Marine and Petroleum Geology, 26*(2), 249-258. https://doi.org/10.1016/j.marpetgeo.2008.02.002

Cartwright, J., Bouroullec, R., James, D., & Johnson, H. (1998). Polycyclic motion history of some Gulf Coast growth faults from high-resolution displacement analysis. *Geology, 26*(9), 819. https://doi.org/10.1130/0091-7613(1998)026<0819:pmhosg>2.3.co;2

Cartwright, J. A., Trudgill, B. D., & Mansfield, C. S. (1995). Fault growth by segment linkage: an explanation for scatter in maximum displacement and trace length data from the Canyonlands Grabens of SE Utah. *Journal of Structural Geology, 17*(9), 1319-1326. https://doi.org/10.1016/0191-8141(95)00033-a

Castelltort, S., Pochat, S., & Van Den Driessche, J. (2004). Using T–Z plots as a graphical method to infer lithological variations from growth strata. *Journal of Structural Geology, 26*(8), 1425-1432. https://doi.org/10.1016/j.jsg.2004.01.002

Chakhmakhchev, A., & Rushworth, P. (2010). *Global overview of recent exploration investment in deepwater - New discoveries, plays and exploration potential.* Paper presented at the AAPG Convention, Calgary, Alberta, Canada.

Chima, K. I., Granjeon, D., Do Couto, D., Leroux, E., Gorini, Ch., Rabineau, M., & Mora-Glukstad, M. (2022). Tectono-stratigraphic evolution of the offshore western Niger Delta from the Cretaceous to present: Implications of delta dynamics and paleo-topography on gravity-driven deformation. *Basin Research, 34*(1), 25-49. https://doi.org/10.1111/bre.12609

Cohen, H. A., & McClay, K. (1996). Sedimentation and shale tectonics of the northwestern Niger Delta front. *Marine and Petroleum Geology, 13*(3), 313-328. https://doi.org/10.1016/0264-8172(95)00067-4

CoreLab (2007). Core Laboratories Indonesia Regional Datasets. In: Corelab (Ed.). Retrieved from: https://corelab.com/irs/cms/docs/Indonesia_Regional_Datasets_Sept2007.pdf

Cullen, A. (2014). Nature and significance of the West Baram and Tinjar Lines, NW Borneo. *Marine and Petroleum Geology, 51*, 197-209. https://doi.org/10.1016/j.marpetgeo.2013.11.010

Cullen, A. B., Zechmeister, M. S., Elmore, R. D., & Pannalal, S. J. (2012). Paleomagnetism of the Crocker Formation, northwest Borneo: Implications for late Cenozoic tectonics. *Geosphere, 8*(5), 1146-1169. https://doi.org/10.1130/GES00750.1

Cullen, A., Reemst, P., Henstra, G., Gozzard, S., & Ray, A. (2010). Rifting of the South China Sea: new perspectives. *Petroleum Geoscience, 16*(3), 273. https://doi.org/10.1144/1354-079309-908

Damuth, J. E. (1994). Neogene gravity tectonics and depositional processes on the deep Niger Delta continental margin. *Marine and Petroleum Geology*, 11(3), 320-346. https://doi.org/10.1016/0264-8172(94)90053-1

Dawers, N. H., Anders, M. H., & Scholz, C. H. (1993). Growth of normal faults: Displacement-length scaling. *Geology*, 21(12), 1107-1110. https://doi.org/10.1130/0091-7613(1993)021<1107:gonfdl>2.3.co;2

Dula, W. F., Jr. (1991). Geometric Models of Listric Normal Faults and Rollover Folds1. *AAPG Bulletin, 75*(10), 1609-1625. https://doi.org/10.1306/0C9B29B1-1710-11D7-8645000102C1865D

Elsley, G. R., & Tieman, H. (2010). A Comparison of Prestack Depth and Prestack Time Imaging of the Paktoa Complex, Canadian Beaufort MacKenzie Basin. In: Wood, L. J. (Ed.), Shale Tectonics (Vol. 93, pp. 79-90): American Association of Petroleum Geologists, Memoir. https://doi.org/10.1306/13231309M933419

Erdi, A., & Jackson, C. A. -L. (2021). What controls salt-detached contraction in the translational domain of the outer Kwanza Basin, offshore Angola? *Basin Research, 33*(3), 1880-1905. https://doi.org/10.1111/bre.12539

Erdi, A., & Jackson, C. A. -L. (2022). Salt-detached strike-slip faulting, Outer Kwanza Basin, Offshore Angola. EarthArxiv. Preprint. https://doi.org/10.31223/X5ND1T Espurt, N., Callot, J.-P., Totterdell, J., Struckmeyer, H., & Vially, R. (2009). Interactions between continental breakup dynamics and large-scale delta system evolution: Insights from the Cretaceous Ceduna delta system, Bight Basin, Southern Australian margin. *Tectonics, 28*(6). https://doi.org/10.1029/2009TC002447 Evamy, B. D., Haremboure, J., Kamerling, P., Knaap, W. A., Molloy, F. A., & Rowlands, P. H. (1978). Hydrocarbon Habitat of Tertiary Niger Delta. *AAPG Bulletin, 62*(1), 1-39. https://doi.org/10.1306/C1EA47ED-16C9-11D7-8645000102C1865D

Fagin, S. (1996). The fault shadow problem: Its nature and elimination. *The Leading Edge*, *15*(9), 1005-1013. https://doi.org/10.1190/1.1437403 Fazlikhani, H., & Back, S. (2012). Temporal and lateral variation in the development of growth faults and growth strata in western Niger Delta, Nigeria. *AAPG Bulletin, 96*(4), 595-614. https://doi.org/10.1306/08291111023

Fazlikhani, H., & Back, S. (2015). The influence of pre-existing structure on the growth of syn-sedimentary normal faults in a deltaic setting, Niger Delta. *Journal of Structural Geology, 73*, 18-32. https://doi.org/10.1016/j.jsg.2015.01.011

Fernández-Ibáñez, F., & Soto, J. I. (2017). Pore pressure and stress regime in a thick extensional basin with active shale diapirism (western Mediterranean). *AAPG Bulletin*, *101*(2), 233–264. https://doi.org/10.1306/07131615228

Francis, A. (2018). A simple gGuide to seismic depth conversion: Part I. *GeoExpro, 15,* 24.

Franke, D., Barckhausen, U., Heyde, I., Tingay, M., & Ramli, N. (2008). Seismic images of a collision zone offshore NW Sabah/Borneo. *Marine and Petroleum Geology, 25*(7), 606-624. https://doi.org/10.1016/j.marpetgeo.2007.11.004

Fuller, M., Haston, R., Lin, J.L., Richter, B., Schmidtke, E., & Almasco, J. (1991). Tertiary paleomagnetism of regions around the South China Sea. *Journal of Southeast Asian Earth Sciences, 6*, 161–184. https://doi.org/10.1016/0743-9547(91)90065-6

Garfunkel, Z. (1984). Large-scale submarine rotational slumps and growth faults in the Eastern Mediterranean. *Marine Geology, 55(3),* 305-324. https://doi.org/10.1016/0025-3227(84)90074-4

Gawthorpe, R. L., Fraser, A. J. & Collier, R. E. L. (1994). Sequence stratigraphy in active extensional basins: implications for the interpretation of ancient basin-fills. *Marine and Petroleum Geology, 11(6), 642-658.* https://doi.org/10.1016/0264-8172(94)90021-3

Ge, H., Jackson, M. P. A., & Vendeville, B. C. (1997). Kinematics and dynamics of salt tectonics driven by progradation. *AAPG Bulletin, 81*(3), 398-423. https://doi.org/10.1306/522B4361-1727-11D7-8645000102C1865D

GEBCO Bathymetric Compilation Group (2020). *The GEBCO_2020 Grid - a continuous terrain model of the global oceans and land*. Retrieved from: http://www.gebco.net

Groshong, R. H., Jr. (2006). 3-D structural geology. A practical guide to quantitative surface and subsurface map interpretation 2nd. Ed. Springer-Verlag, Berlin, 400 pp. https://doi.org/10.1007/978-3-540-31055-6

Hall, R. (2009). The Eurasian SE Asian margin as a modern example of an accretionary orogen. In: Cawood, P. A., & Kröner, A. (Eds.), *Earth Accretionary Systems in Space and Time*. The Geological Society, London, Special Publications, 318, 351–372. https://doi.org/10.1144/SP318.13

Hall, R. (2012). Late Jurassic–Cenozoic reconstructions of the Indonesian region and the Indian Ocean. *Tectonophysics, 570-571*, 1-41. https://doi.org/10.1016/j.tecto.2012.04.021

Hall, R. (2013). Contraction and extension in northern Borneo driven by subduction rollback. *Journal of Asian Earth Sciences, 76*, 399-411. https://doi.org/10.1016/j.jseaes.2013.04.010

Hall, R. (2019). The subduction initiation stage of the Wilson cycle. In: Wilson, R. A., Houseman, G. A., McCaffrey, K. J. W., Doré, A. G., & Buiter, S. J. H.(Eds.), *Fifty Years of the Wilson Cycle Concept in Plate Tectonics*. Geological Society, London, Special Publications, 470, 415–437. https://doi.org/10.1144/SP470.3

Hall, R., & Nichols, G. J. (2002). Cenozoic sedimentation and tectonics in Borneo: climatic influences on orogenesis. In: Jones, S. J., & Frostick, L. (Eds.), *Sediment Flux to Basins: Causes, Controls and Consequences.* Geological Society, London, Special Publication, 191, 5–22. https://doi.org/10.1144/GSL.SP.2002.191.01.02

Hansen, J. P. V., Cartwright, J. A., Huuse, M., & Clausen, O. R. (2005). 3D seismic expression of fluid migration and mud remobilization on the Gjallar Ridge, offshore mid-Norway. *Basin Research, 17*(1), 123-139. https://doi.org/10.1111/j.1365-2117.2005.00257.x

Harding, T. P. (1990). Identification of wrench faults using subsurface structural data: Criteria and pitfalls. *AAPG Bulletin, 74*(10), 1590-1609. https://doi.org/10.1306/0C9B2533-1710-11D7-8645000102C1865D

Heriyanto, N., Satoto, W., & Sardjono, S. (1992). *An overview of hydrocarbon maturity and its migration aspects in Bunyu Island, Tarakan Basin.* Paper presented at the Indonesian Petroleum Association, 21st Annual Convention and Exhibition Jakarta, Indonesia.

Hidayati, S., Guritno, E., Argenton, A., Ziza, W., & Del Campana, I. (2007). *Re-Visited Structural Framework of the Tarakan Sub-Basin Northeast Kalimantan-Indonesia.* Paper presented at the Proceedings, Indonesian Petroleum Association, 31st Annual Convention and Exhibition

Hudec, M. R., & Soto, J I. (2021). Piercement Mechanisms for Mobile Shales. *Basin Research, 33,* 2862–2882. https://doi.org/10.1111/bre.12586

Hutchison, C.S., 1996. The 'Rajang Accretionary Prism' and 'Lupar Line' problem of Borneo. In: Hall, R., & Blundell, D. J. (Eds.), *Tectonic Evolution of SE Asia*. Geological Society, London, Special Publication*,* 106, 247–261. https://doi.org/10.1144/GSL.SP.1996.106.01.16

Hutchison, C. S. (2005). *Geology of North West Borneo: Sarawak, Brunei and Sabah*. Amsterdam, Elsevier.

Hutchison, C. S., Bergman, S. C., Swauger, D. A., & Graves, J. E. (2000). A Miocene collisional belt in north Borneo: uplift mechanism and isostatic adjustment quantified by thermochronology. *Journal of the Geological Society, 157*(4), 783-793. https://doi.org/10.1144/jgs.157.4.783

Imber, J., Childs, C., Nell, P. A. R., Walsh, J. J., Hodgetts, D., & Flint, S. (2003). Hanging wall fault kinematics and footwall collapse in listric growth fault systems. *Journal of Structural Geology, 25*(2), 197-208. https://doi.org/10.1016/s0191-8141(02)00034-2

Indrajaya, H., Susanti, D. N., Usman, T. K., Wicaksono, A. F., Sijabat, H., Wahyudin, M., & Sugiri. (2016). *Integrated interpretation of borehole and geophysical data for fault configuration and its implication to hydrocarbon distribution in Bunyu Area, Tarakan Basin.* Paper presented at the Indonesian Petroleum Association.

Jackson, C. A. L., Bell, R. E., Rotevatn, A., & Tvedt, A. B. M. (2017). Techniques to determine the kinematics of synsedimentary normal faults and implications for fault growth models. In: Childs, C., Holdsworth, R. E., Jackson, C. A.-L., Manzocchi, T., Walsh, J. J., & Yielding, G. (Eds.), *The Geometry and Growth of Normal Faults.* Geological Society, London, Special Publications, 439, 187-217. https://doi.org/10.1144/sp439.22

Jackson, C. A. L., & Rotevatn, A. (2013). 3D seismic analysis of the structure and evolution of a salt-influenced normal fault zone: A test of competing fault growth models. *Journal of Structural Geology, 54*, 215-234. https://doi.org/10.1016/j.jsg.2013.06.012

Jackson, M. P. A., & Hudec, M. R. (2017). *Salt tectonics: principles and practice*. Cambridge, Cambridge University Press.

Johnson, P. W., & Hansen, K. (1987). *Method for calibrating stacking velocities for use in time-depth conversion*. Paper presented at the Offshore Technology Conference. https://doi.org/10.4043/5403-MS

Kopf, A. J. (2002). Significance of mud volcanism. *Reviews of Geophysics, 40*(2), 2-1-2-52. https://doi.org/10.1029/2000RG000093

Lacoste, A., Vendeville, B. C., Mourgues, R., Loncke, L., & Lebacq, M. (2012). Gravitational instabilities triggered by fluid overpressure and downslope incision – Insights from analytical and analogue modelling. *Journal of Structural Geology, 42*, 151-162. https://doi.org/10.1016/j.jsg.2012.05.011

Lentini, M. R., & Darman, H. (1996). *Aspects of the Neogene tectonic history and hydrocarbon geology of the Tarakan Basin.* Paper presented at the Indonesian Petroleum Association, 25th Annual Convention and Exhibition, Indonesia.

Levell, B., Argent, J., Doré, A. G., & Fraser, S. (2010). Passive margins: overview. In: Vining, B. A., & Pickering, S. C (Eds.), *Petroleum Geology: From Mature Basins to New Frontiers.* Geological Society, London, Petroleum Conference series, 7, 823–830. https://doi.org/10.1144/0070823

Li, Ch., Luo, X., Zhang, L., Fan, C., Xu, Ch., Liu, A., Li, H., Li, J., & Lei, Y. (2022). New understanding of overpressure responses and pore pressure prediction: Insights from the effect of clay mineral transformations on mudstone compaction. *Engineering Geology, 297*, 106493. https://doi.org/10.1016/j.enggeo.2021.106493

Madon, M., Kim, Ch. L., & Wong, R. (2013). The structure and stratigraphy of deepwater Sarawak, Malaysia: Implications for tectonic evolution. *Journal of Asian Earth Sciences, 76*, 312–333. https://doi.org/10.1016/j.jseaes.2013.04.040

Mandl, G., & Crans, W. (1981). Gravitational gliding in deltas. In: McClay, K. R., & Price, N. J. (Eds.), *Thrust and nappe tectonics*. Geological Society, London, Special Publications, 9, 41–54. https://doi.org/10.1144/GSL.SP.1981.009.01.05

Mansfield, C. S., & Cartwright, J. (1996). High resolution fault displacement mapping from three-dimensional seismic data: evidence for dip linkage during fault growth. *Journal of Structural Geology, 18*(2-3), 249-263. https://doi.org/10.1016/S0191-8141(96)80048-4

Maulin, H. B., Sapiie, B., & Gunawan, I. (2021). Analisis Sesar Tumbuh Pada Sistem Tektonik Delta Tersier di Subcekungan Tarakan, Kalimantan Utara. *Bulletin of Geology, 5*(2), 570-579.

McClay, K. R. (1990). Extensional fault systems in sedimentary basins: a review of analogue model studies. *Marine and Petroleum Geology, 7*(3), 206-233. https://doi.org/10.1016/0264-8172(90)90001-W

McClay, K., Dooley, T., & Zamora, G. (2003). Analogue models of delta systems above ductile substrates. In: Van Rensbergen, P., Hillis, R. R., Maltman, A. J., & Morley, C. K. (Eds.) *Subsurface sediment mobilization*. Geological Society, London, Special Publications, 216, 411–428. https://doi.org/10.1144/GSL.SP.2003.216.01.27

McGrath, A. G., & Davison, I. (1995). Damage zone geometry around fault tips. *Journal of Structural Geology, 17*(7), 1011-1024. https://doi.org/10.1016/0191-8141(94)00116-H

Miller, K. G., Browning, J. V., Schmelz, W. J., Kopp, R. E., Mountain, G. S., & Wright, J. D. (2020). Cenozoic sea-level and cryospheric evolution from deep-sea geochemical and continental margin records. *Science Advances, 6*(20), eaaz1346. https://doi.org/10.1126/sciadv.aaz1346

Mitchum, R. M., Jr., Vail, P. R., & Sangree, J. B. (1977). Seismic stratigraphy and global changes of sea level, Part 6: Stratigraphic interpretation of seismic reflection patterns in depositional sequences. In: Payton, C. E. (Ed.), *Seismic Stratigraphy — Applications to Hydrocarbon Exploration* . American Association of Petroleum Geologists, Memoir, 26, 117–133. https://doi.org/10.1306/M26490C8

Morley, C. K. (2003). Mobile shale related deformation in large deltas developed on passive and active margins. In: Van Rensbergen, P., Hillis, R.R., Maltman, A.J., & Morley, C.K. (Eds.) *Subsurface sediment mobilization*. Geological Society, London, Special Publications, 216, 335-357. https://doi.org/10.1144/GSL.SP.2003.216.01.22

Morley, C. K. (2007). Development of crestal normal faults associated with deepwater fold growth. *Journal of Structural Geology, 29*(7), 1148-1163. https://doi.org/10.1016/j.jsg.2007.03.016

Morley, C. K., & Guerin, G. (1996). Comparison of gravity-driven deformation styles and behavior associated with mobile shales and salt. *Tectonics, 15*(6), 1154-1170. https://doi.org/10.1029/96TC01416

Morley, C. K., Westaway, R., 2006. Subsidence in the super-deep Pattani and Malay basins of Southeast Asia: a coupled model incorporating lower-crustal flow in response to post-rift sediment loading. *Basin Research*, 18, 51–84. https://doi.org/10.1111/j.1365-2117.2006.00285.x

Moss, S. J., Carter, A., Baker, S., & Hurford, A. J. (1998). A Late Oligocene tectono-volcanic event in East Kalimantan and the implications for tectonics and sedimentation in Borneo. *Journal of the Geological Society, 155*(1), 177–192. https://doi.org/10.1144/gsjgs.155.1.0177

Mourgues, R., Lecomte, E., Vendeville, B., & Raillard, S. (2009). An experimental investigation of gravity-driven shale tectonics in progradational delta. *Tectonophysics, 474*(3), 643-656. https://doi.org/10.1016/j.tecto.2009.05.003

Netherwood, R., & Wight, A. (1992). *Structurally-controlled, linear reefs in a Pliocene delta-front setting, Tarakan Basin, Northeast Kalimantan*. Paper presented at the Carbonate Rocks and Reservoirs of Indonesia: A Core Workshop.

Peacock, D. C. P., & Sanderson, D. J. (1991). Displacements, segment linkage and relay ramps in normal fault systems. *Journal of Structural Geology, 13*(6), 721-733. https://doi.org/10.1016/0191-8141(91)90033-F

Pochat, S., Castelltort, S., Van Den Driessche, J., Besnard, K., & Gumiaux, C. (2004). A simple method of determining sand/shale ratios from seismic analysis of growth faults: An example from upper Oligocene to lower Miocene Niger Delta deposits. *AAPG Bulletin, 88*(10), 1357-1367. https://doi.org/10.1306/bltn03117

Pubellier, M., & Morley, C. K. (2014). The basins of Sundaland (SE Asia): Evolution and boundary conditions. *Marine and Petroleum Geology, 58*, 555-578. https://doi.org/10.1016/j.marpetgeo.2013.11.019

Putra, P. R., Tasiyat, Sapiie, B., & Ramadhan, A. M. (2017). *Pore pressure prediction and its relationship to structural style in Offshore Tarakan Sub-Basin, Northeast Kalimantan.* Paper presented at the Indonesian Petroleum Association, 41st Annual Convention and Exhibition Jakarta, Indonesia.

Rangin, C., & Silver, E. (1991). Neogene tectonic evolution of the Celebes-Sulu Basins : New insights from Leg 124 drilling. *In:* Silver, E. A., Rangin, C., von Breymann, M. T., et al. (Eds.), *Proc. ODP, Sci. Results,* 124: College Station, TX (Ocean Drilling Program), 51–63. https://doi.org/10.2973/odp.proc.sr.124.122.1991

Rider, M. H. (1978). Growth faults in Carboniferous of Western Ireland. *AAPG Bulletin, 62*(11), 2191-2213. https://doi.org/10.1306/C1EA53BE-16C9-11D7-8645000102C1865D

Santos Betancor, I., & Soto, J. I. (2015). 3D geometry of a shale-cored anticline in the western South Caspian Basin (offshore Azerbaijan). *Marine and Petroleum Geology, 67*, 829-851. https://doi.org/10.1016/j.marpetgeo.2015.06.012

Sapin, F., Ringenbach, J.-C., Rives, T., & Pubellier, M. (2012). Counter-regional normal faults in shale-dominated deltas: Origin, mechanism and evolution. *Marine and Petroleum Geology, 37*(1), 121-128. https://doi.org/10.1016/j.marpetgeo.2012.05.001

Sapiie, B., Furqan, T. A., Septama, E., Wardaya, P. D., & Gunawan, I. (2021) Mechanism of gravity-driven deformation using sandbox modeling: A case study of the Tarakan Sub-Basin, East Kalimantan. Paper presented at the Indonesian Petroleum Association, 45th Annual Convention and Exhibition Jakarta, Indonesia.

Schlüter, H. U., Hinz, K., & Block, M. (1996). Tectono-stratigraphic terranes and detachment faulting of the South China Sea and Sulu Sea. *Marine Geology, 130*(1), 39-78. https://doi.org/10.1016/0025-3227(95)00137-9

Silver, E., & Rangin, C. (1991). Development of the Celebes Basin in the context of Western Pacific marginal basin history. *In:* Silver, E. A., Rangin, C., von Breymann, M. T., et al. (Eds.), *Proc. ODP, Sci. Results,* 124: College Station, TX (Ocean Drilling Program), 39–49. https://doi.org/10.2973/odp.proc.sr.124.121.1991

Soto, J. I., Fernández-Ibáñez, F., Talukder, A. R., & Martínez-García, P. (2010). Miocene Shale Tectonics in the Northern Alboran Sea (Western Mediterranean). In: Wood, L. J. (Ed.), *Shale Tectonics.* American Association of Petroleum Geologists, Memoirs, 93, 119–144. https://doi.org/10.1306/13231312M933422

Soto, J. I., Heidari, M., & Hudec, M. R. (2021a). Proposal for a mechanical model of mobile shales. *Scientific Reports, 11*(1), 23785. https://doi.org/10.1038/s41598-021-02868-x

Soto, J. I., Hudec, M. R., Mondol, N. H., & Heidari, M. (2021b). Shale transformations and physical properties—Implications for seismic expression of mobile shales. *Earth-Science Reviews*, 103746. https://doi.org/10.1016/j.earscirev.2021.103746

Sylvester, A G. (1988). Strike-slip faults. *GSA Bulletin, 100*(11), 1666-1703. https://doi.org/10.1130/0016-7606(1988)100<1666:SSF>2.3.CO;2

Tearpock, D. J. & Bischke, R.E. (2002). Applied subsurface geological mapping with structural methods, 2nd. Ed. Pearson Education, 864 pp.

Van Bemmelen, R. W. (1949). *The Geology of Indonesia*: The Government Printing Office, The Hague.

Van Rensbergen, P., & Morley, C. K. (2000). 3D Seismic study of a shale expulsion syncline at the base of the Champion delta, offshore Brunei and its implications for the early structural evolution of large delta systems. *Marine and Petroleum Geology, 17*(8), 861-872. https://doi.org/10.1016/S0264-8172(00)00026-X

Van Rensbergen, P., Morley, C. K., Ang, D. W., Hoan, T. Q., & Lam, N. T. (1999). Structural evolution of shale diapirs from reactive rise to mud volcanism: 3D seismic data from the Baram delta, offshore Brunei Darussalam. *Journal of the Geological Society, 156*(3), 633-650. https://doi.org/10.1144/gsjgs.156.3.0633

Van Rensbergen, P., & Morley, C. K. (2003). Re-evaluation of mobile shale occurrences on seismic sections of the Champion and Baram deltas, offshore Brunei. In: Van Rensbergen, P., Hillis, R. R., Maltman, A. J., & Morley, C. K. (Eds.) *Subsurface sediment mobilization*. Geological Society, London, Special Publications, 216, 395–409. https://doi.org/10.1144/GSL.SP.2003.216.01.26

Van Hattum, M. W. A., Hall, R., Pickard, A. L., & Nichols, G. J. (2013). Provenance and geochronology of Cenozoic sandstones of northern Borneo. *Journal of Asian Earth Sciences, 76*, 266-282. https://doi.org/10.1016/j.jseaes.2013.02.033

Walsh, J. J., Bailey, W. R., Childs, C., Nicol, A., & Bonson, C. G. (2003). Formation of segmented normal faults: a 3-D perspective. *Journal of Structural Geology, 25*(8), 1251-1262. https://doi.org/10.1016/s0191-8141(02)00161-x

Walsh, J. J., & Watterson, J. (1988). Analysis of the relationship between displacements and dimensions of faults. *Journal of Structural Geology, 10*(3), 239–247. https://doi.org/10.1016/0191-8141(88)90057-0

Walsh, J. J., Watterson, J., Bailey, W. R., & Childs, C. (1999). Fault Relays, bends, and branch-lines. *Journal of Structural Geology, 21*(8–9), 1019–1026. https://doi.org/10.1016/S0191-8141(99)00026-7

Watkinson, I. M., & Hall, R. (2017). Fault systems of the eastern Indonesian triple junction: Evaluation of Quaternary activity and implications for seismic hazards. In: Cummins, P. R., & Meilano, I. (Eds.), *Geohazards in Indonesia: Earth Science for Disaster Risk Reduction* (Vol. 441, pp. 71–120): The Geological Society of London. https://doi.org/10.1144/SP441.8

Wight, A. W. R., Hare, L. H., & Reynolds, J. R. (1993). Tarakan Basin, NE Kalimantan, Indonesia: a century of exploration and future hydrocarbon potential. *Bulletin of the Geological Society of Malaysia, 33*, 263-288. https://doi.org/10.7186/bgsm33199319

Ze, T., & Alves, T. M. (2019). Impacts of data sampling on the interpretation of normal fault propagation and segment linkage. *Tectonophysics, 762*, 79-96. https://doi.org/10.1016/j.tecto.2019.03.013

Zhang, J., Wu, S., Hu, G., Yue, D., Xu, Z., Chen, Ch., Zhang, K., Wang, J., & Wen, S. (2021). Role of Shale Deformation in the structural development of a deepwater gravitational system in the Niger Delta. *Tectonics, 40*(5), e2020TC006491. https://doi.org/10.1029/2020TC006491

Table

Table 1

Data	TBB-11 (Southern area)	TBN-10 (Northern area)
Date of acquisition and processing	2011-2012	2011-2012
Type/Processing	3D Kirchhoff Pre-Stack Time Migration (PSTM) seismic data	
Total area (km^2)	1316	1625
Water depth (m)	200-500	15-400
Inline orientation	N-S trending	NE-SE trending
Seismic dimension (m)	49039 x 60036	45290 x 70909
Vertical sample rate (ms)	2	2
Line spacing (m)	25	25
Vertical resolution	25 m at seabed	21 m at seabed
	250 m at 8710 ms	208 m at 7069 ms

Table 2

Horizon	Interval Velocity (m/s)	Time	Seismic Character	Interpretation
H7	1500-3010	Upper Pleistocene (~0.012 Ma)	Parallel, very strong positive amplitude reflector observed in the S. It is locally as a chaotic, moderately medium-to-weak reflector in the NE.	Top of the youngest angular unconformity, being shown by onlap or downlap of overlying stratal (labelled E4; Figs 3 and 4) . Associated to rollover folds within strata in the S.
H6	1700-3100	Lower Pleistocene (~1.8 Ma)	Parallel-to-sub parallel, low-to-medium positive amplitude reflector across the study area. It shows locally diverge eastward in the SE.	Angular unconformity in the SE, being shown by onlap or downlap of overlying stratal (labelled E3; Figs 3 and 4).
H5	2100-3100	Pliocene (~2.6 Ma)	Parallel-to-wavy, very strong positive amplitude reflector in the S. Moderately chaotic reflector in the NE, and weak reflector and diverge eastward in the NE and SE.	Angular unconformity in the SE, being shown by onlap or downlap of overlying stratal (labelled E2; Figs 3 and 4; c.f. Horizon II; Levell, 1987; Horizon A; Franke et al., 2008).
H4	2400-3200	Upper most Miocene (~6.3 Ma)	Parallel strong positive amplitude reflector in the S. A moderate medium-weak, wavy and chaotic reflector in the NE and SE.	Angular unconformity in the SE, being shown by onlap or downlap of overlying stratal (Figs 3 and 4). Associated to rollover folds in the S.
H3	3000-3200	Upper Miocene? (~8.2 Ma?)	Parallel-to-wavy, strong negative amplitude reflector.	Recording distribution rollover fold within strata in the northwest area.

H2	2900-3300	Middle Miocene? (~13.8 Ma?)	Parallel-to-sub parallel, strong positive amplitude reflector in the N. It is a chaotic, moderate medium-strong reflector in the S.	Angular unconformity in the central part, being shown by onlap or downlap of overlying stratal (labelled E1; Fig 5).
TMB (Mobile shale)	3100-3500	Middle Miocene? (~14.8 Ma?)	Parallel-to-sub parallel negative amplitude reflector that marks transition between overburden and underlying mobile-shales. The mobile shales are seen as chaotic, weak-to-moderate amplitude reflections or as a domain with loss of reflectivity. Locally,its internal fabric shows cross-cutting reflections (label X in Figs 4 and 5).	Seismic facies of the mobile-shales is either interpreted due to overpressure and/or to severe destruction of the fabric by deformation at critical-state conditions (Soto et al., 2021b). It cannot be excluded the existence of relict fabrics and/or seismic noise due to inaccurate seismic processing and acquisition (Elsley and Tieman, 2011; Li and Mitra, 2020).
H1	3300-3500	Eocene-to-late Early Miocene (~16-33 Ma)	Positive reflection in the S and N, while it is discontinously imaged in the centre.	Top of syn-rift unit (South China Sea Unconformity; Cullen, 2010, 2014) of Early Miocene or Middle Miocene age (Madon, 1999; Hutchison, 2005; Madon et al., 2013). This reflection marks the base of mobile-shales and is also the top of deep half grabens bounded by thick-skinned extensional faults.

Table 3

Name	Shale Roller (SR)	Shale Anticline (SA)	Mud Diapir (MD)	Mud Volcano (MV)
Example	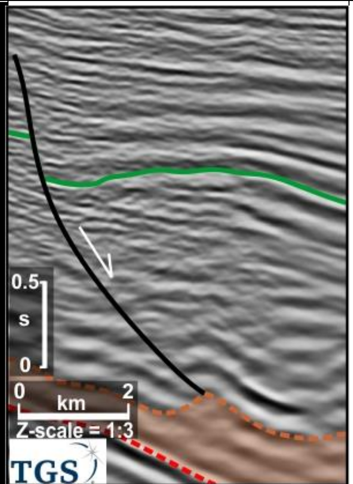		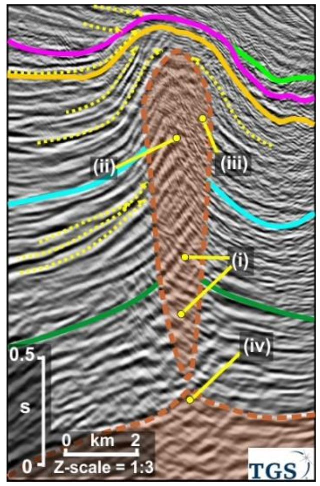	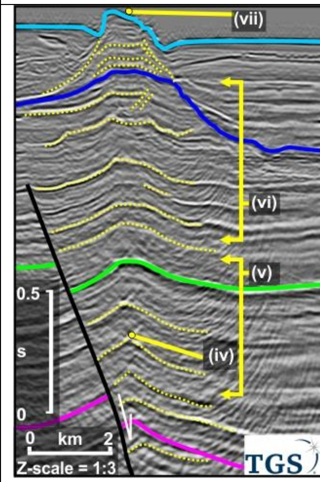
Seismic character	Broadly weak, sub-parallel-to-dipping chaotic reflector above mobile shale.	Chaotic, weak-to-moderate, amplitude reflections of mobile shale forming a structural high (label iv) with continuous supra shale reflections.	Cross-cutting chaotic reflections rise from the high (label i), being overlaid by significantly upturn, isolated low-amplitude, chaotic reflections (label ii). The chaotic reflections limited by a transitional zone of weak reflections (label iii).	Conical edifice with some internal reflectivity, usually placed above a deep anticline. Not clear feeders, although high angle normal faults are commonly seen below the mud volcano.
Diagnostic description	An asymmetric, low amplitude triangular profile, comprising of a gentle and a relative steep-dipping flank that bound depocenter. On map view, it is reflected by an elongated thick mobile shale, parallel to the bounding normal fault.	A low amplitude, large wavelength anticline. On map view, it is accompanied by an elongated domain of thick mobile shales.	H2-H3 are pierced by a mud-diapir body. On map view, it is seen as an elliptical domain that is defined by folding that affect H2 and H3.	The reflections form a mounded structure between intra H5 and seabed (label v-vii). On map view, it is reflected by an asymmetric elliptical conical edifice usually seen between H5 and seabed in the north.
Trend	NE-to-N			
Length (km)	≤ 80	≤ 12	≤ 11	≤ 3
Width (km)	≤ 5	≤ 4.3	≤ 2	≤ 1.5
Height (s)	≤ 1.2 (2.8 km)	≤ 0.6 (1.5 km)	≤ 3 (5 km)	≤ 1.9 (2.6 km)
Supra-shale faults association	Rollover and basinward-dipping or counter-regional normal fault with a listric and planar geometry.	N/A	N/A	Normal faults below the mud volcano

Driving mechanism	Reactive piercement (e.g. Hudec and Soto, 2021).	Contraction and/or horizontal flow of mobile shale (c.f. Santos Betancor and Soto, 2015; Back and Morley, 2016).	Piercement produced by fluid migration along fractures, generated above the fold crest (H3-H4) (e.g. Santos Betancor and Soto, 2015; Hudec and Soto, 2021).	Piercement produced by fluid and shale migration along fractures in the lower interval (H5-intra H7) (e.g. Hudec and Soto, 2021), being followed upward by H7-seabed (e.g. Hansen et al., 2005).

Key: (H7) Upper Pleistocene; (H6) Lower Pleistocene; (H5) Pliocene; (H4) Upper most Miocene; (H3) Upper Miocene; (H2) Middle Miocene; Top Mobile Shale (TMB); (H1) Early Miocene

Table 4

Name	Example	Diagnostic description	Dip/ Plunge direction	Length (km)	Dip (o)	Max. throw (s)	Fault	Stra-tigraphic Architecture	Processes
Shale-detached normal fault (labelled SN)	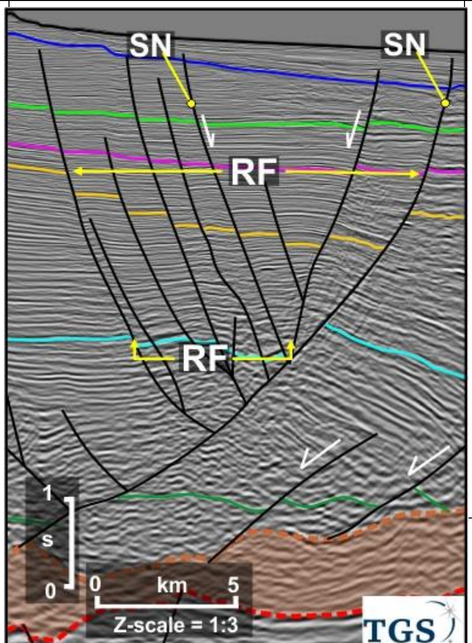	Listric or planar normal growth faults: Listric faults are detached along a surface below nearly horizontal stratum. In map view, they have both concave and convex geometries.	Basinward and landward (counter-regional)	≤ 74	30-86	≤ 2.8	Normal offset generally at H2-H6. The lower fault tips are within the mobile shales	SU1-SU6 thicken toward fault plane, forming a fault-bound depocenter.	Reactive piercement (e.g. Morley and Guerin, 1996; Hudec and Soto, 2021). Progressive prograding sedimentary loading (sedimentary-driven mechanism; e.g. Ge et al., 1997; Jackson et al., 2015, Back and Morley, 2016)
		Planar normal faults form symmetric and asymmetric grabens, above roll-over folds. In map view, the faults are parallel to the master listric faults.	Basinward and landward	≥ 1.9	60-85	≤ 0.1	Normal offset at H2-H6. The lower fault tips either die out downward into the supra shale sequence or form a	SU3-SU6 subtle thicken toward fault plane	Outer arc bending due to folding (e.g. Hongbin and Suppe, 1992; Imber et al, 2003; Erdi and Jackson, 2021).

							physical-linkage with the listric fault		
Rollover fold (labelled RF)		Anticlines affecting an asymmetric wedge thickening toward the master fault. In map view, they are characterized by a broad-to-wide geometry (i.e. ratio of amplitude and half-wavelength=0.21-0.53) where axial fold surface are oriented parallel to the shale-detached normal fault. Locally they have oblique linkage folds.	Basinward and landward	≤ 43	≤ 8 away and ≤ 13 toward master faults	N/A	N/A	SU2-5 thicken and bend toward the listric fault, and commonly thin outward.	Differential rate between sedimentation and fault slip (e.g. Dula, 1991; Hongbin and Suppe, 1992; Imber et al, 2003; Fazlikhani and Back, 2015).

Key: (H7) Upper Pleistocene (H6) Lower Pleistocene (H5) Pliocene (H4) Uppermost Miocene (H3) Upper Miocene (H2) Middle Miocene Top Mobile Shale (TMB) (H1) Early Miocene

Figures

Figure 1

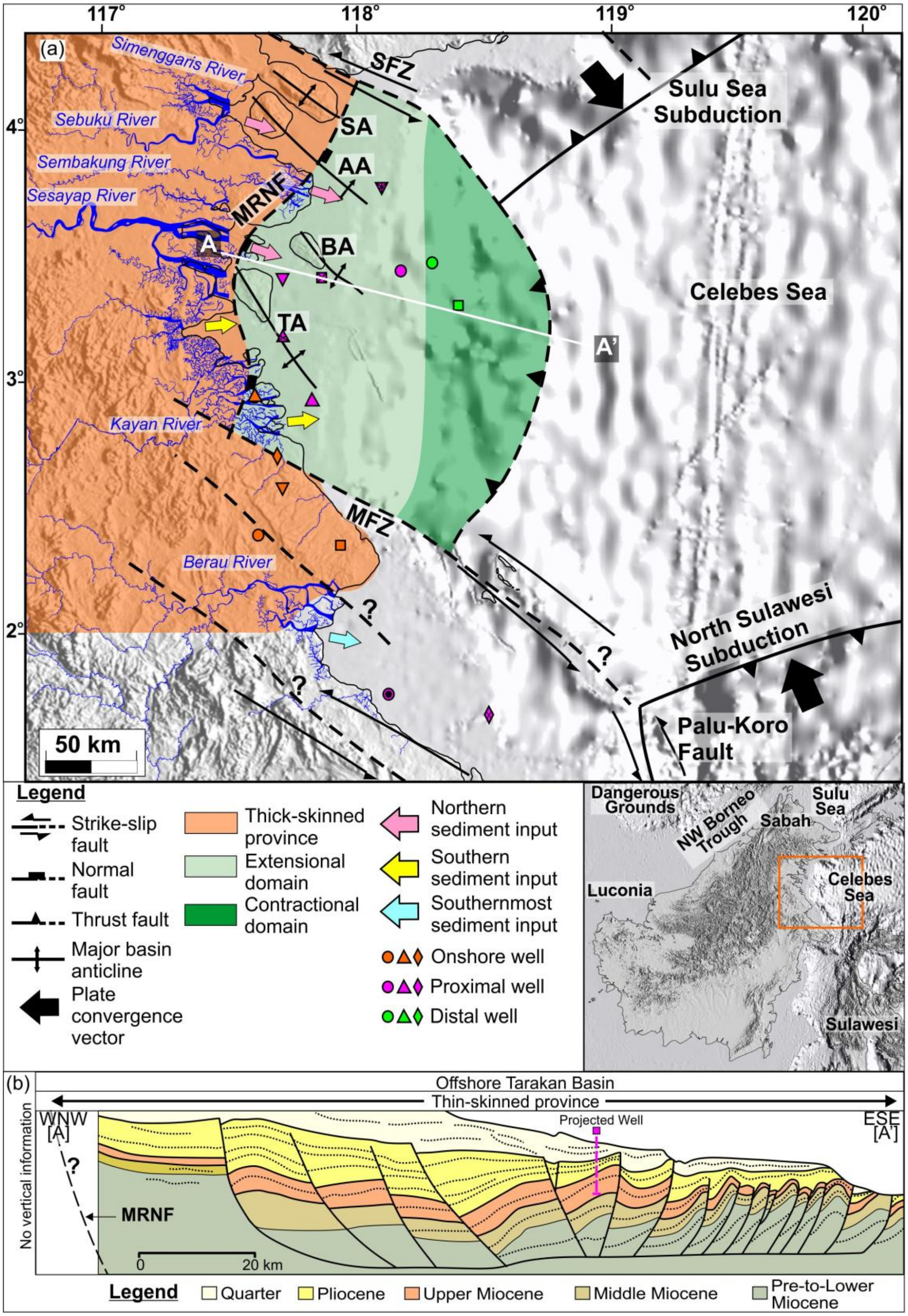

Figure 2

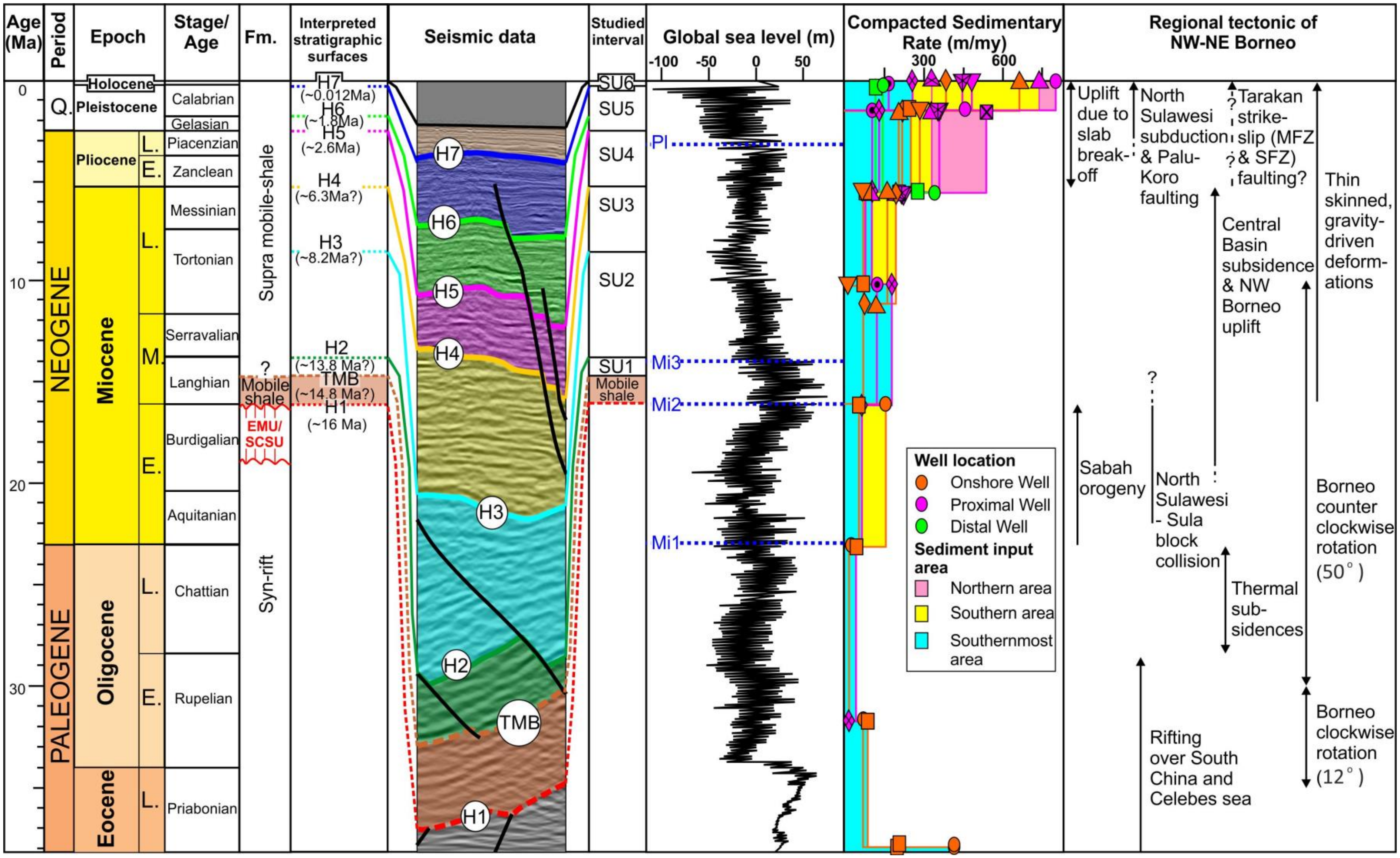

Age (Ma)
Period
Epoch
Stage/ Age
Fm.
Interpreted stratigraphic surfaces
Seismic data
Studied interval
Global sea level (m)
-100 -50 0 50
Compacted Sedimentary Rate (m/my)
300 600
Regional tectonic of NW-NE Borneo
0
10
20
30
Q.
NEOGENE
PALEOGENE
Holocene
Pleistocene
Pliocene
Miocene
Oligocene
Eocene
L.
E.
M.
Calabrian
Gelasian
Piacenzian
Zanclean
Messinian
Tortonian
Serravalian
Langhian
Burdigalian
Aquitanian
Chattian
Rupelian
Priabonian
Supra mobile-shale
?
Mobile shale
EMU/ SCSU
Syn-rift
H7 (~0.012Ma)
H6 (~1.8Ma)
H5 (~2.6Ma)
H4 (~6.3Ma?)
H3 (~8.2Ma?)
H2 (~13.8 Ma?)
TMB (~14.8 Ma?)
H1 (~16 Ma)
H7
H6
H5
H4
H3
H2
TMB
H1
SU6
SU5
SU4
SU3
SU2
SU1
Mobile shale
Pl
Mi3
Mi2
Mi1
Well location
Onshore Well
Proximal Well
Distal Well
Sediment input area
Northern area
Southern area
Southernmost area
Uplift due to slab break-off
North Sulawesi subduction & Palu-Koro faulting
Tarakan strike-slip (MFZ & SFZ) faulting?
Thin skinned, gravity-driven deform-ations
Central Basin subsidence & NW Borneo uplift
Sabah orogeny
North Sulawesi - Sula block collision
Thermal sub-sidences
Borneo counter clockwise rotation (50°)
Borneo clockwise rotation (12°)
Rifting over South China and Celebes sea

1148 Figure 3

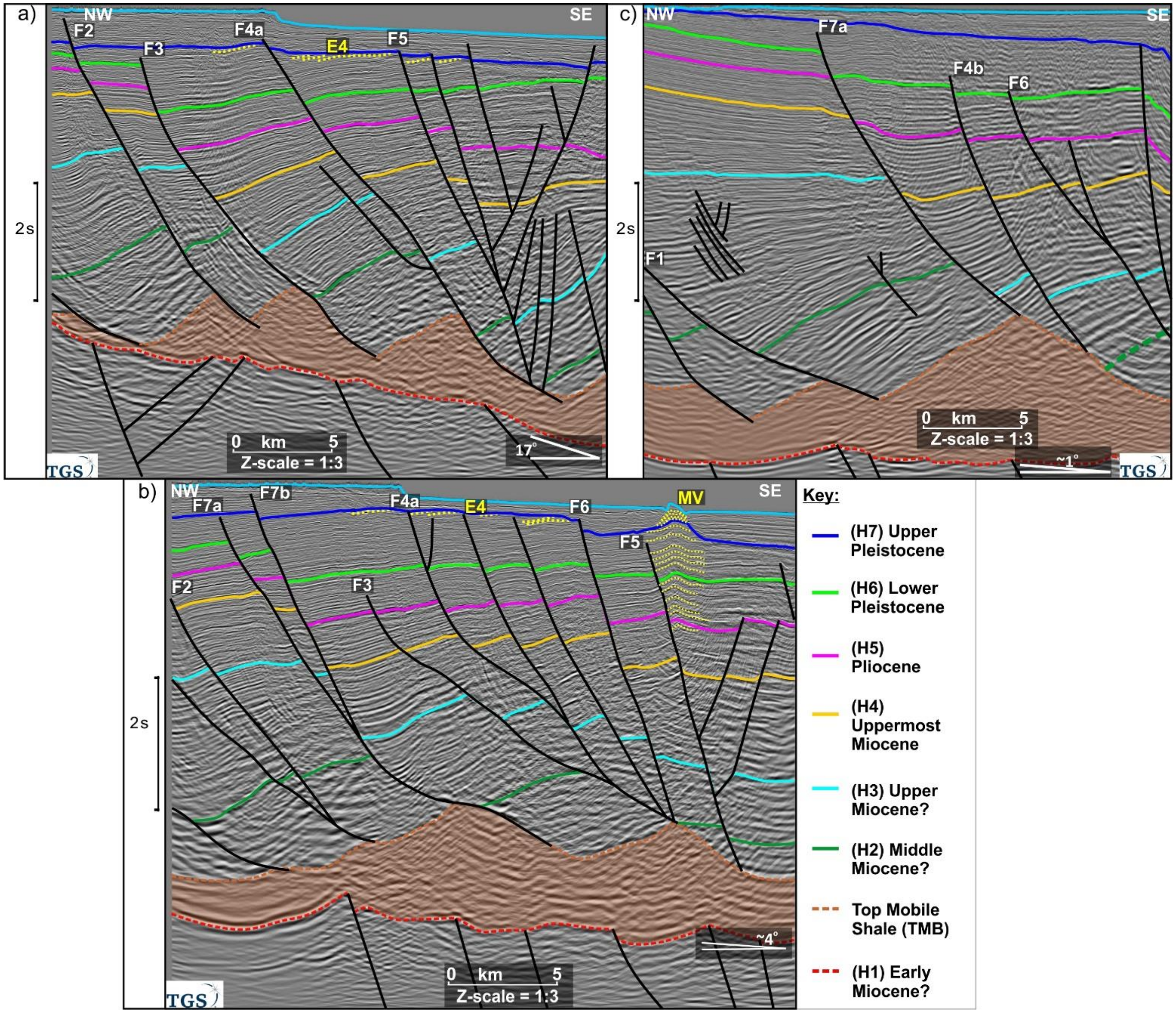

1149

Figure 4

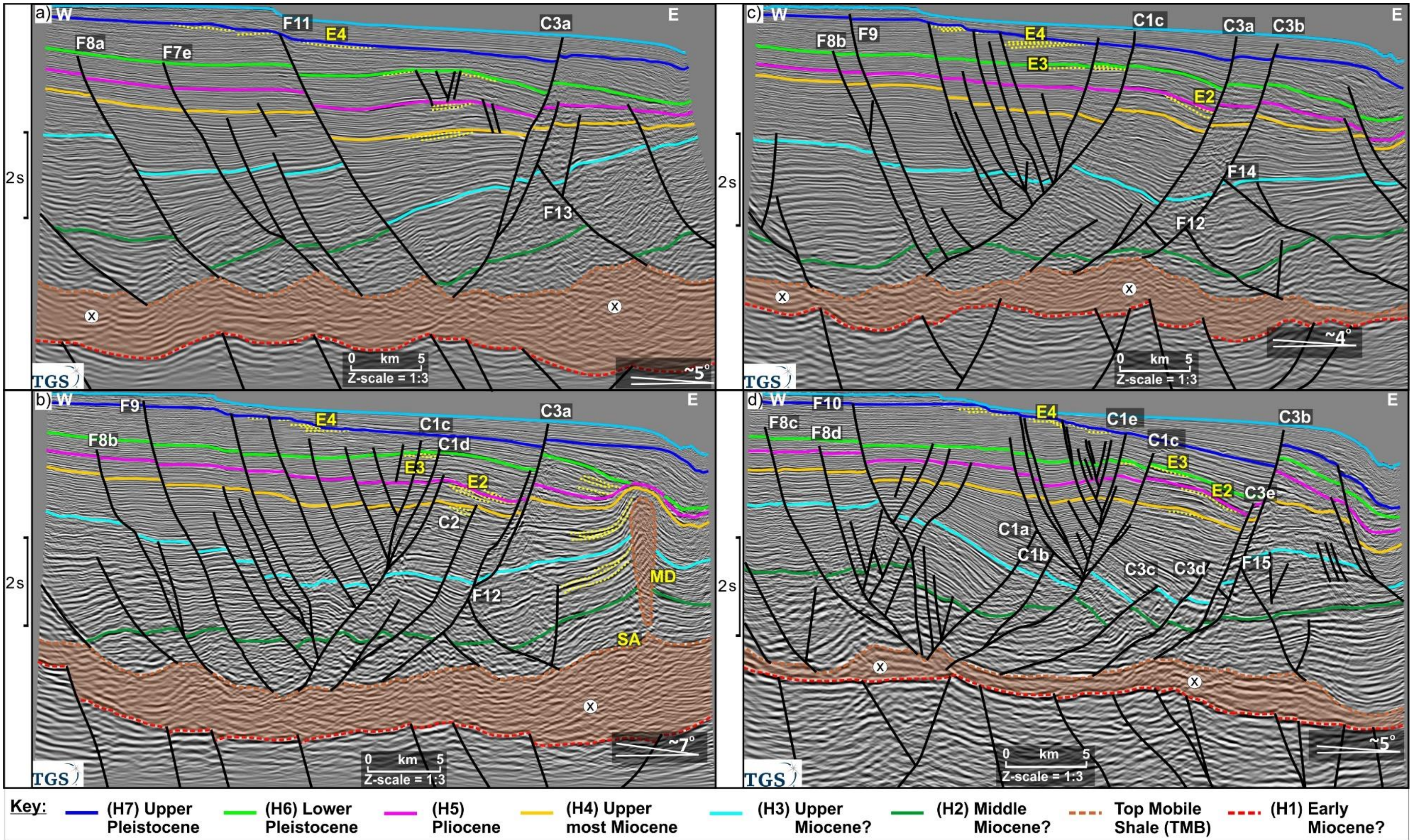

a) W
E
F11
E4
C3a
F8a
F7e
F13
2s
0 km 5
Z-scale = 1:3
~5°
TGS
c) W
E
F8b
F9
E4
E3
C1c
C3a
C3b
E2
F14
F12
2s
0 km 5
Z-scale = 1:3
~4°
TGS
b) W
E
F9
F8b
E4
C1c
C1d
E3
E2
C3a
C2
F12
MD
SA
2s
0 km 5
Z-scale = 1:3
~7°
TGS
d) W
E
F10
F8c
F8d
E4
C1e
C1c
E3
E2
C3e
C3b
C1a
C1b
C3c
C3d
F15
2s
0 km 5
Z-scale = 1:3
~5°
TGS
Key:
(H7) Upper Pleistocene
(H6) Lower Pleistocene
(H5) Pliocene
(H4) Upper most Miocene
(H3) Upper Miocene?
(H2) Middle Miocene?
Top Mobile Shale (TMB)
(H1) Early Miocene?

Figure 5

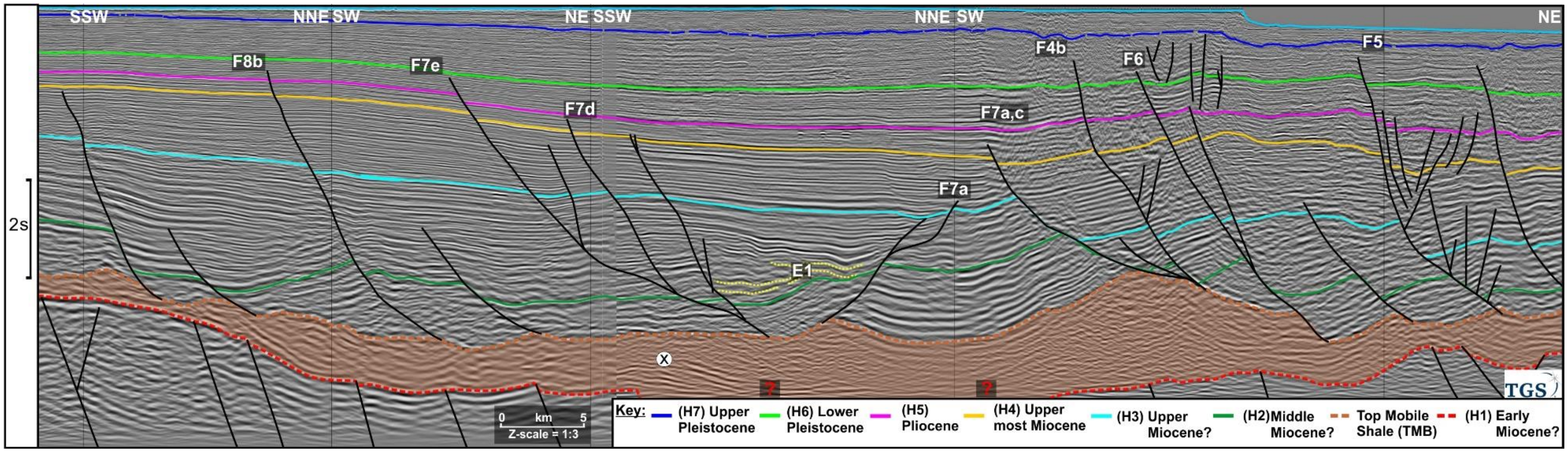

SSW
NNE SW
NE SSW
NNE SW
NE
F8b
F7e
F7d
F7a,c
F7a
F4b
F6
F5
E1
2s
0 km 5
Z-scale = 1:3
TGS
Key:
(H7) Upper Pleistocene
(H6) Lower Pleistocene
(H5) Pliocene
(H4) Upper most Miocene
(H3) Upper Miocene?
(H2) Middle Miocene?
Top Mobile Shale (TMB)
(H1) Early Miocene?

1154 Figure 6

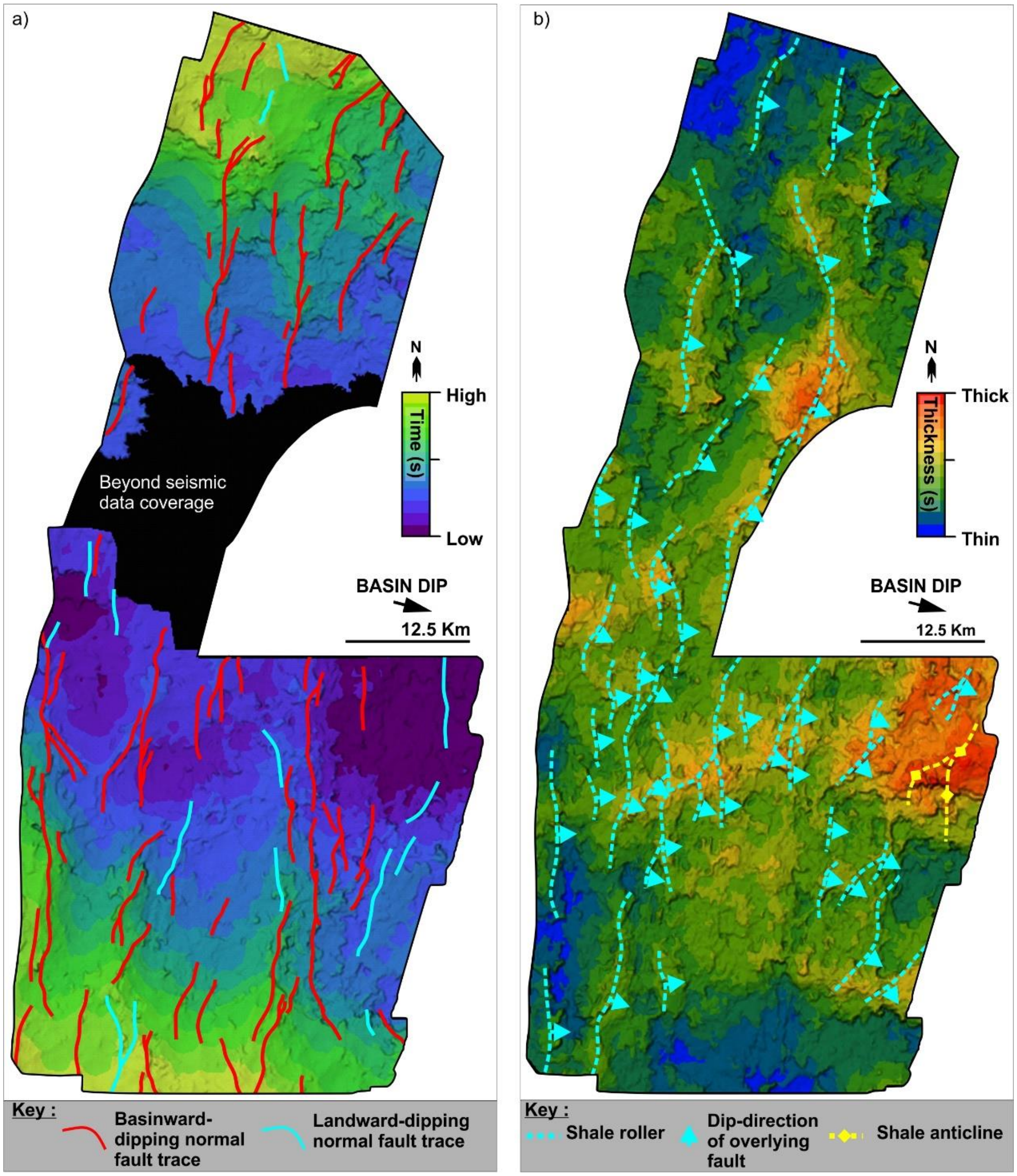

1155

1156 Figure 7

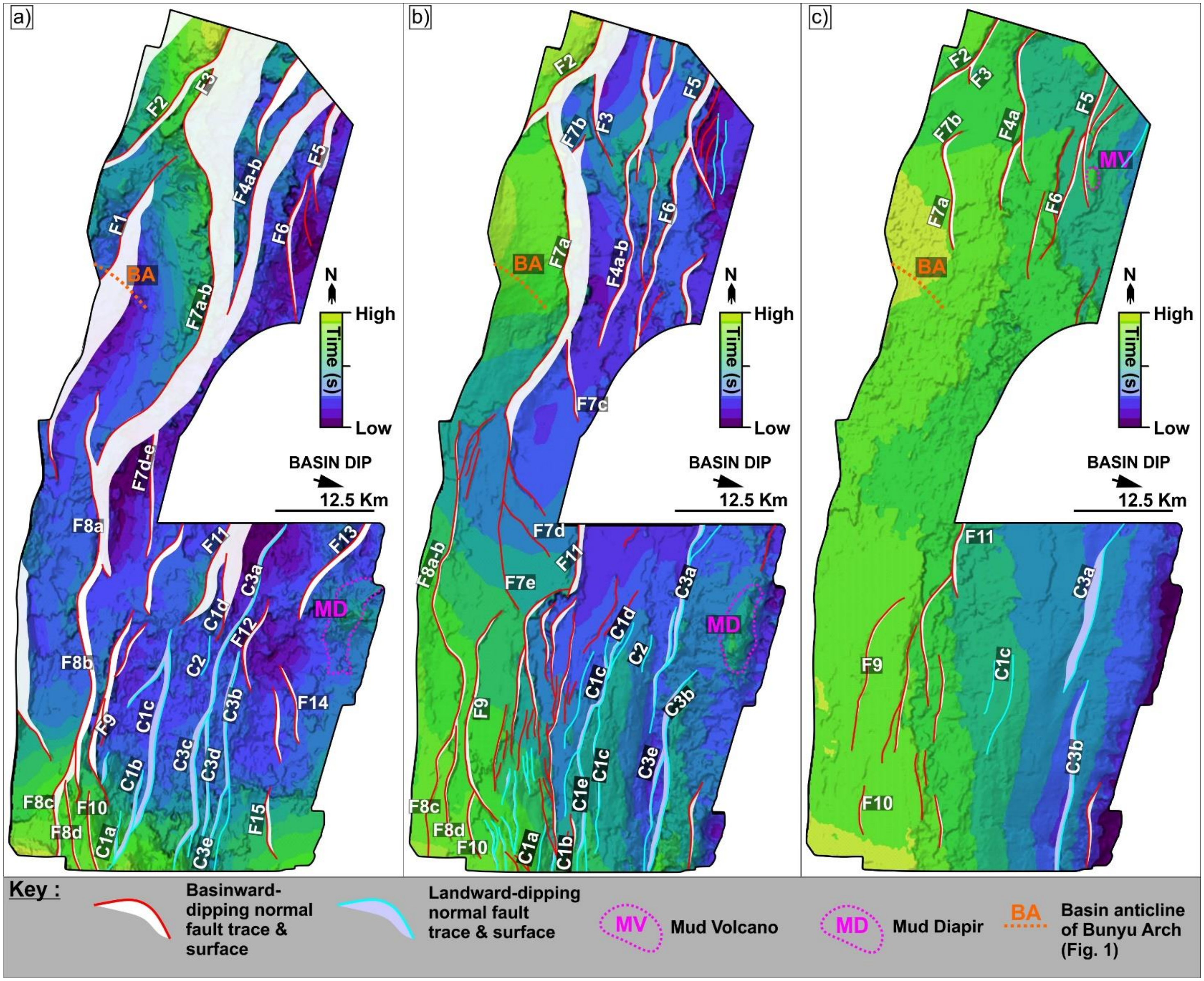

1157

Figure 8

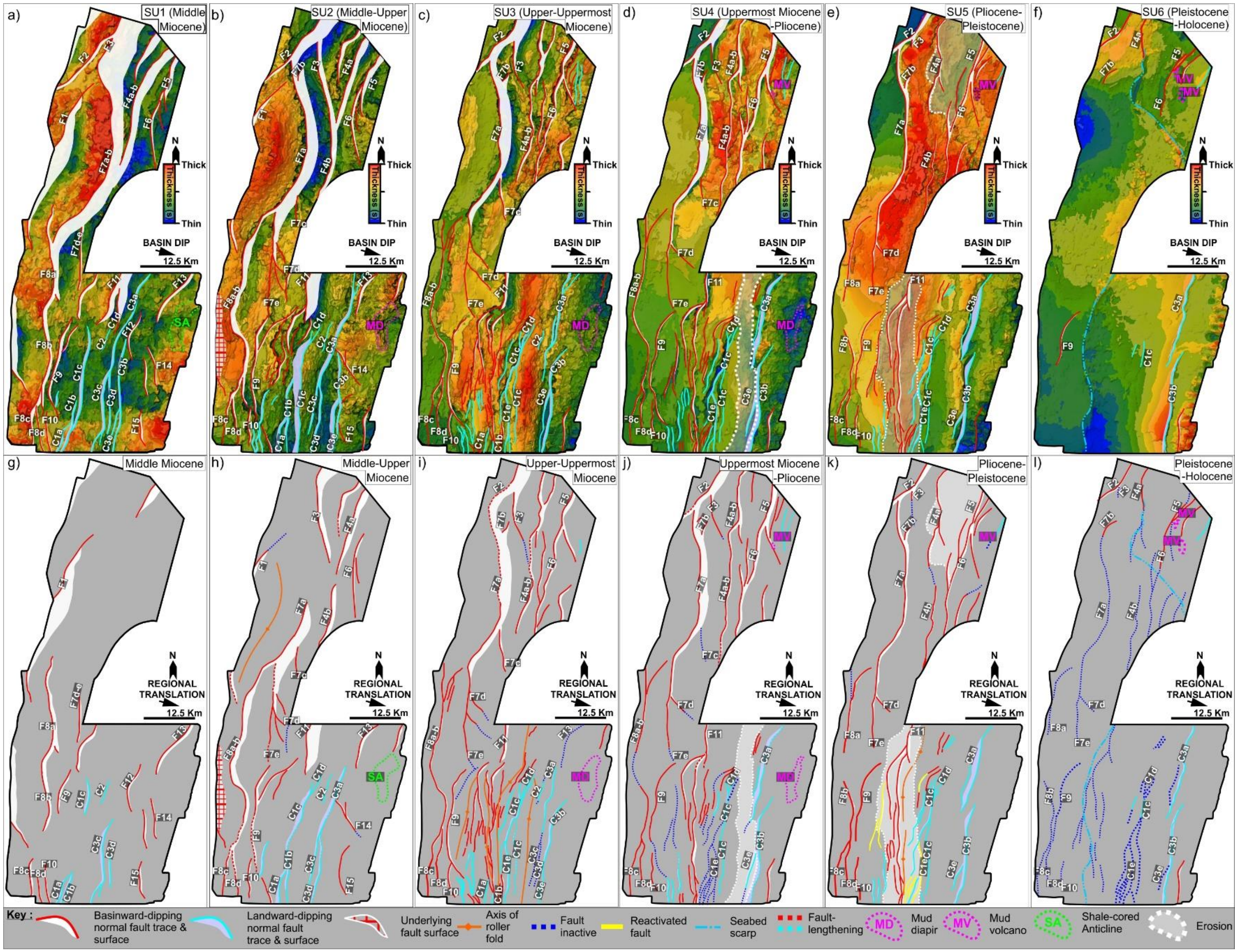
a)
SU1 (Middle Miocene)
b)
SU2 (Middle-Upper Miocene)
c)
SU3 (Upper-Uppermost Miocene)
d)
SU4 (Uppermost Miocene -Pliocene)
e)
SU5 (Pliocene-Pleistocene)
f)
SU6 (Pleistocene -Holocene)
N
Thick
Thickness (s)
Thin
BASIN DIP
12.5 Km
g)
Middle Miocene
h)
Middle-Upper Miocene
i)
Upper-Uppermost Miocene
j)
Uppermost Miocene -Pliocene
k)
Pliocene-Pleistocene
l)
Pleistocene -Holocene
REGIONAL TRANSLATION
Key :
Basinward-dipping normal fault trace & surface
Landward-dipping normal fault trace & surface
Underlying fault surface
Axis of roller fold
Fault inactive
Reactivated fault
Seabed scarp
Fault-lengthening
MD
Mud diapir
MV
Mud volcano
SA
Shale-cored Anticline
Erosion

1160 Figure 9

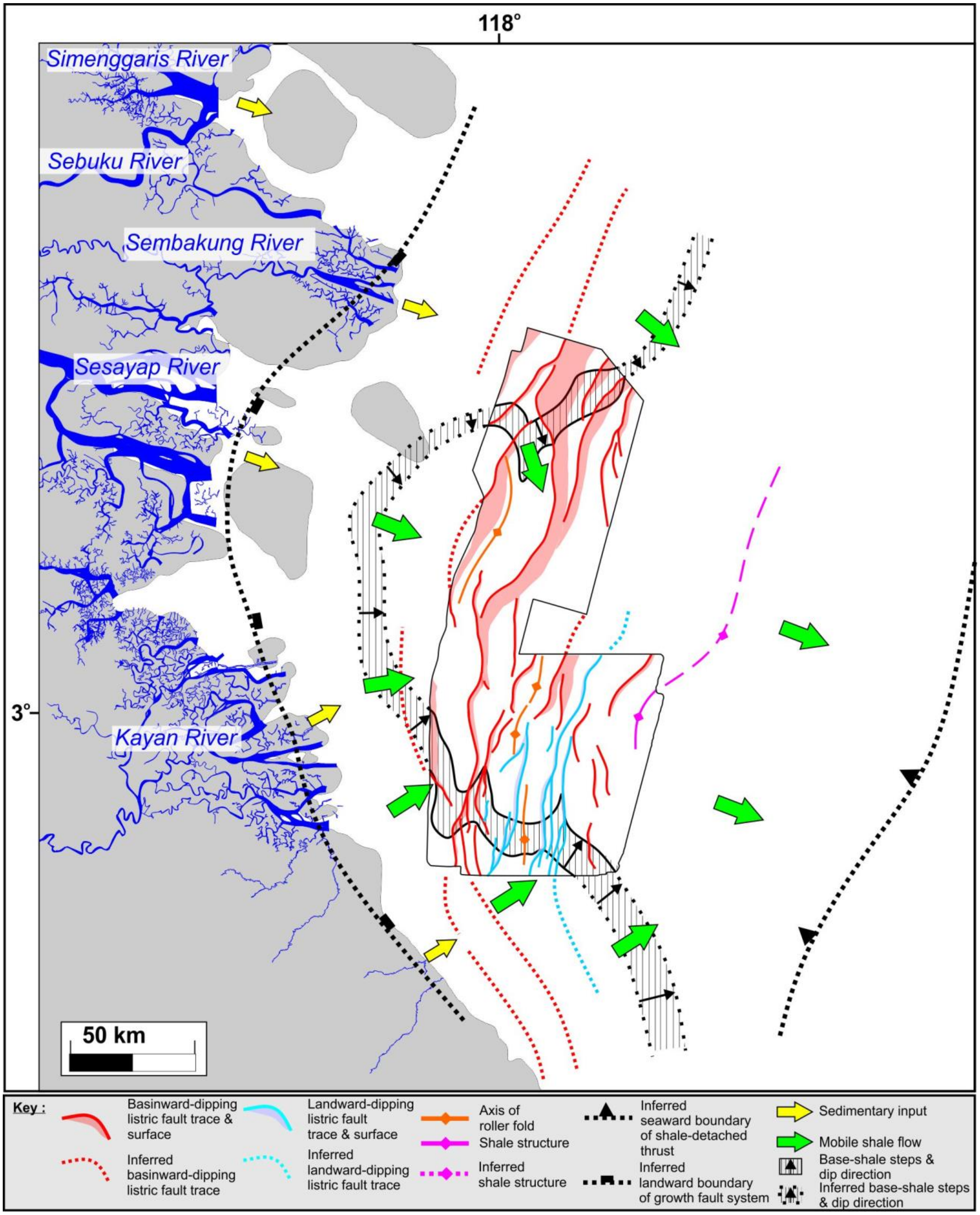

1161

Supporting Information for:

DEFORMATION OF A SHALE-DOMINATED DELTA: TARAKAN BASIN, OFFSHORE INDONESIA

Aurio Erdi[1,2], Christopher A-L. Jackson[1], Juan I. Soto[3, #]

[1]Basin Research Group (BRG), Department of Earth Science and Engineering, Imperial College, London, United Kingdom

[2]National Research and Innovation Agency (BRIN), Indonesia

[3]Bureau of Economic Geology, Jackson School of Geosciences, The University of Texas at Austin, University Station, Box X, Austin, Texas, 78713-8924, USA

[#]On leave of absence from: Departamento de Geodinámica, Universidad de Granada, Avenida de Fuente Nueva s/n, 18071 Granada, Spain

Content of this file

Table S1. A larger version of Table 3 in main text, showing summary of the diagnostic seismic characteristic of the shale structures between shelf-edge and upper slope of Tarakan Basin, offshore Indonesia. Seismic data courtesy of TGS.

Table S2. A larger version of Table 4 in main text, showing summary of principal characteristics of the supra-shale faults in the area between shelf-edge and upper slope of Tarakan Basin, offshore Indonesia. Seismic data courtesy of TGS.

Appendix S1**.** Uninterpreted seismic cross-sections

Figure S1. (a-c) Uninterpreted margin-perpendicular (parallel to regional base-mobile shale and bulk translation direction) seismic profiles of figure 3 in main text across northern area. Seismic data courtesy of TGS.

Figure S2. (a-d) Uninterpreted margin-perpendicular (parallel to regional base-mobile shale and bulk translation direction) seismic profiles of figure 4 in main text across southern area. Seismic data courtesy of TGS.

Figure S3. Margin-parallel (i.e. normal to regional base-mobile shale and bulk translation direction) seismic profiles of figure 5 in main text. Seismic data courtesy of TGS.

Appendix S2. A large version of isopach and interpretative sketch maps

Figure S4. (a-l) A larger version of figure 8 in main text, showing overburden isopach and their interpretative sketch maps that illustrate evolution of shale and supra-shale structures during Middle Miocene until Holocene.

Table S 1. A larger version of Table 3 in main text, showing summary of the diagnostic seismic characteristic of the shale structures between shelf-edge and upper slope of Tarakan Basin, offshore Indonesia.

Name	Shale roller (SR)	Shale anticline (SA)	Mud diapir (MD)	Mud volcano (MV)
Example	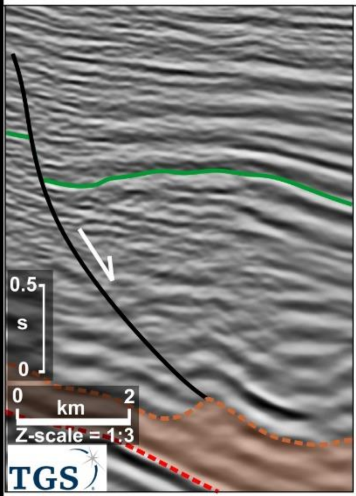	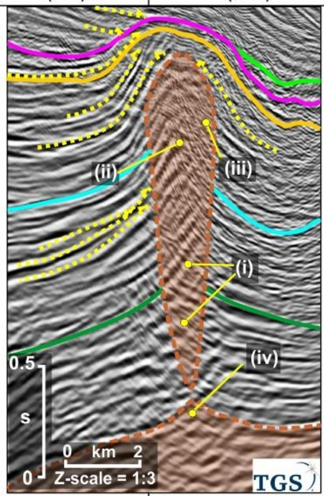		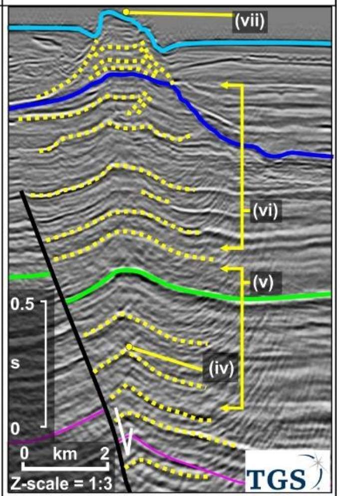
Seismic character	Broadly weak, sub-parallel-to-dipping chaotic reflections above mobile shale.	Chaotic, weak-to-moderate, amplitude reflections of mobile shale forming a structural high (label iv) with continous supra shale reflections.	Cross-cutting chaotic reflections rise from the high (label i), being overlaid by significantly upturn, isolated low-amplitude, chaotic reflections (label ii). The chaotic reflections limited by a transitional zone of weak reflections (label iii).	Conic edifice with some internal reflectifity, usually placed above a deep anticline. Not clear feeders, although high angle normal faults are commonly seen below the mud volcano.
Diagnostic description	An asymmetric, low amplitude triangular profile, comprising of a gentle and a relative steep-dipping flank that bound depocentre. On map view, it is reflected by an elongated thick mobile shale, parallel to the bounding normal fault.	Low amplitude, a large wavelength anticline. On map view, it is accompanied by an ellongated domain of thick mobile shales.	H2-H3 are pierced by a mud-diapir body. On map view, it is seen as an elliptical domain that is defined by folding that affect H2 and H3.	The reflections form a mounded structure between intra H5 and seabed (label v-vii). On map view, it is reflected by an asymmetric elliptical conical edifice usually seen between H5 and seabed in the north.
Trend	NE-to-N			
Length (km)	≤ 80	≤ 12	≤ 11	≤ 3
Width (km)	≤ 5	≤ 4.3	≤ 2	≤ 1.5
Height(s)	≤ 1.2 (2.8 km)	≤ 0.6 (1.5 km)	≤ 3 (5 km)	≤ 1.9 (2.6 km)
Supra-shale association	Rollover and basinward- or landward-dipping normal fault with a listric and planar geometry.	N/A	N/A	Normal faults below the mud volcano
Driving mechanism	Reactive piercement (e.g. Hudec and Soto, 2021).	Contraction and/ or horizontal flow of mobile shale (c.f.Santos Bentancor and Soto, 2015; Back and Morley., 2016).	Piercement produced by fluid migration along fractures, generated above the fold crest (H3-H4) (e.g. Santos Bentancor and Soto, 2015; Hudec and Soto, 2021).	Piercement produced by fluid and shale migration along fractures in the lower interval (H5-intra H7) (e.g. Hudec and Soto, 2021), being followed upward by H7-seabed (e.g. Hansen et al, 2005).

Key: (H7) Upper Pleistocene; (H6) Lower Pleistocene; (H5) Pliocene; (H4) Upper most Miocene; (H3) Upper Miocene; (H2) Middle Miocene; Top Mobile Shale (TMB); (H1) Early Miocene

Table S 2. A larger version of Table 4 in main text, showing summary of principal characteristics of the supra-shale faults in the area between shelf-edge and upper slope of Tarakan Basin, offshore Indonesia.

Name	Example	Diagnostic description	Dip/Plunge direction	Length (km)	Dip (o)	Max. throw (s)	Fault	Strati-graphic architecture	Processes
Shale-detached normal fault (labeled SN)	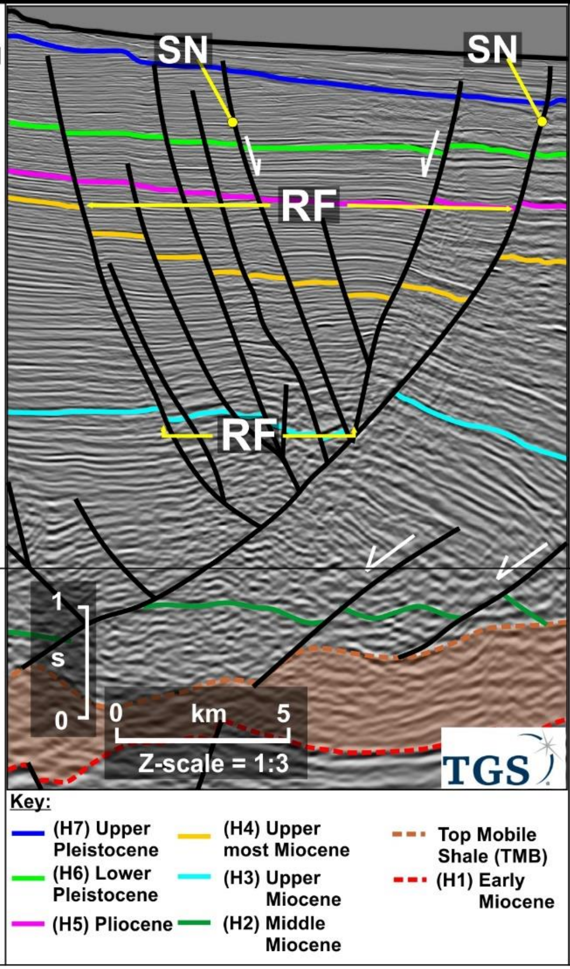	Listric or planar normal growth faults: Listric faults are detached along a surface below nearly horizontal strata. In map view, they have both concave and convex geometries.	Basinward and landward (counter-regional)	≤ 74	30-86	≤ 2.8	Normal offset generally at H2-H6. The lower fault tips are within the mobile shales	SU1-SU6 thicken toward fault plane, forming a fault-bound depocenter.	Reactive piercement (e.g. Morley and Guerin, 1996; Hudec and Soto, 2021). Progressive prograding sedimentary loading (sedimentary-driven mechanism; e.g. Ge et al., 1997; Jackson et al., 2015, Back and Morley, 2016)
		Planar normal faults form symmetric and asymmetric grabens, above roll-over folds. In map view, the faults are parallel to the master listric faults.	Basinward and landward	≥ 1.9	60-85	≤ 0.1	Normal offset at H2-H6. The lower fault tips either die out downward into the supra shale sequence or form a physical-linkage with the listric fault	SU3-SU6 subtle thicken toward fault plane	Outer arc bending due to folding (e.g. Hongbin and Suppe, 1992; Imber et al, 2003; Erdi and Jackson, 2021).
Rollover fold (labelled RF)		Anticlines affecting an asymmetric wedge thickening toward the master fault. In map view, they are charac-terized by a broad-to-wide geometry (i.e. ratio of amplitude and half-wavelength=0.21-0.53) where axial fold surface are oriented paralel to the shale-detached normal fault. Locally they have oblique linkage folds.	Basinward and landward	≤ 43	≤ 8 away and ≤ 13 toward master faults	N/A	N/A	SU2-5 thicken and bend toward the listric fault, and commonly thin outward.	Differential rate between sedimentation and fault slip (e.g. Dula, 1991; Hongbin and Suppe, 1992; Imber et al, 2003; Fazlikhani and Back, 2015).

Appendix S1. Uninterpreted seismic cross-sections

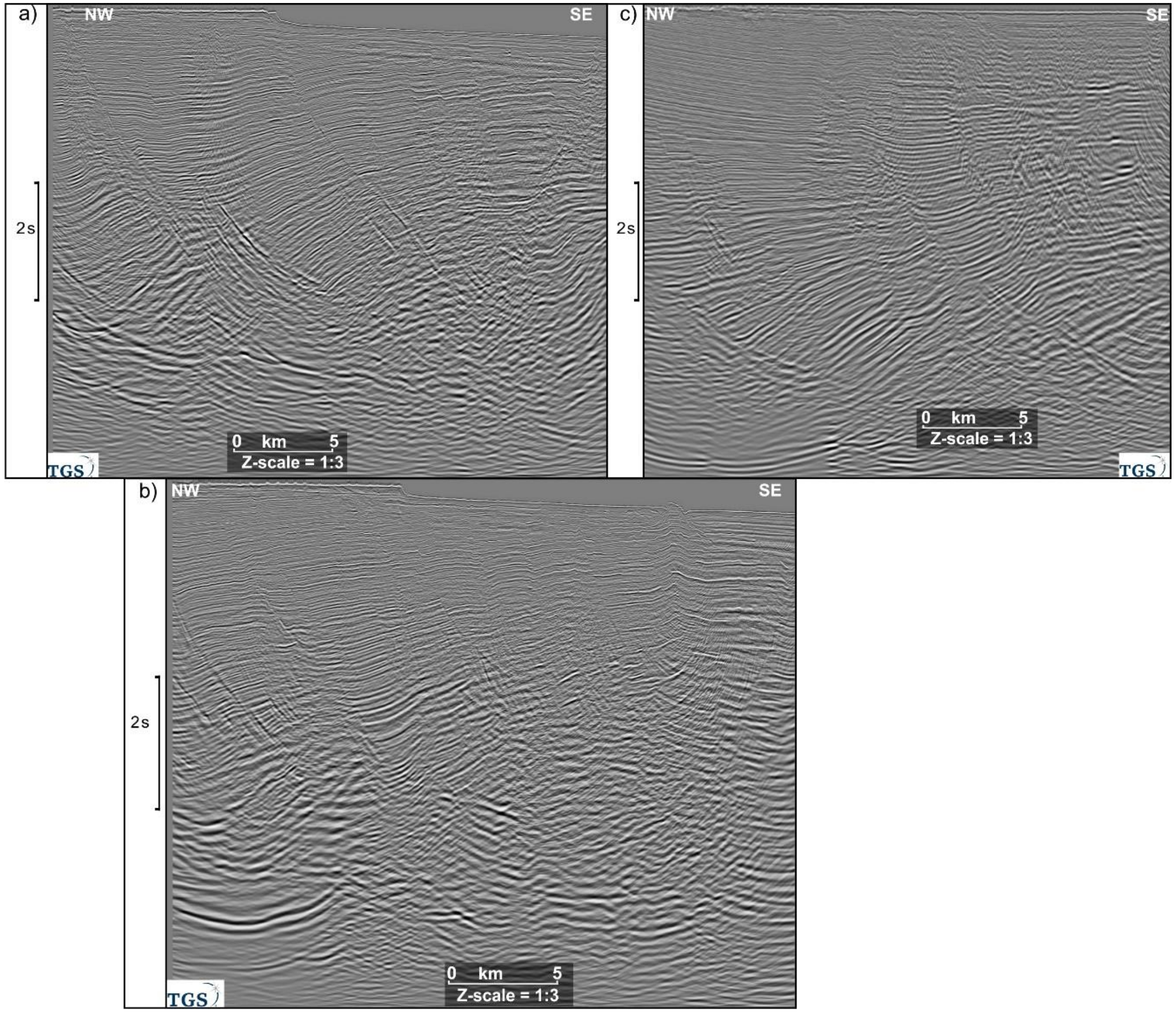

Figure S 1. (a-c) Uninterpreted margin-perpendicular (parallel to regional base-mobile shale and bulk translation direction) seismic profiles of figure 3 in main text across northern area.

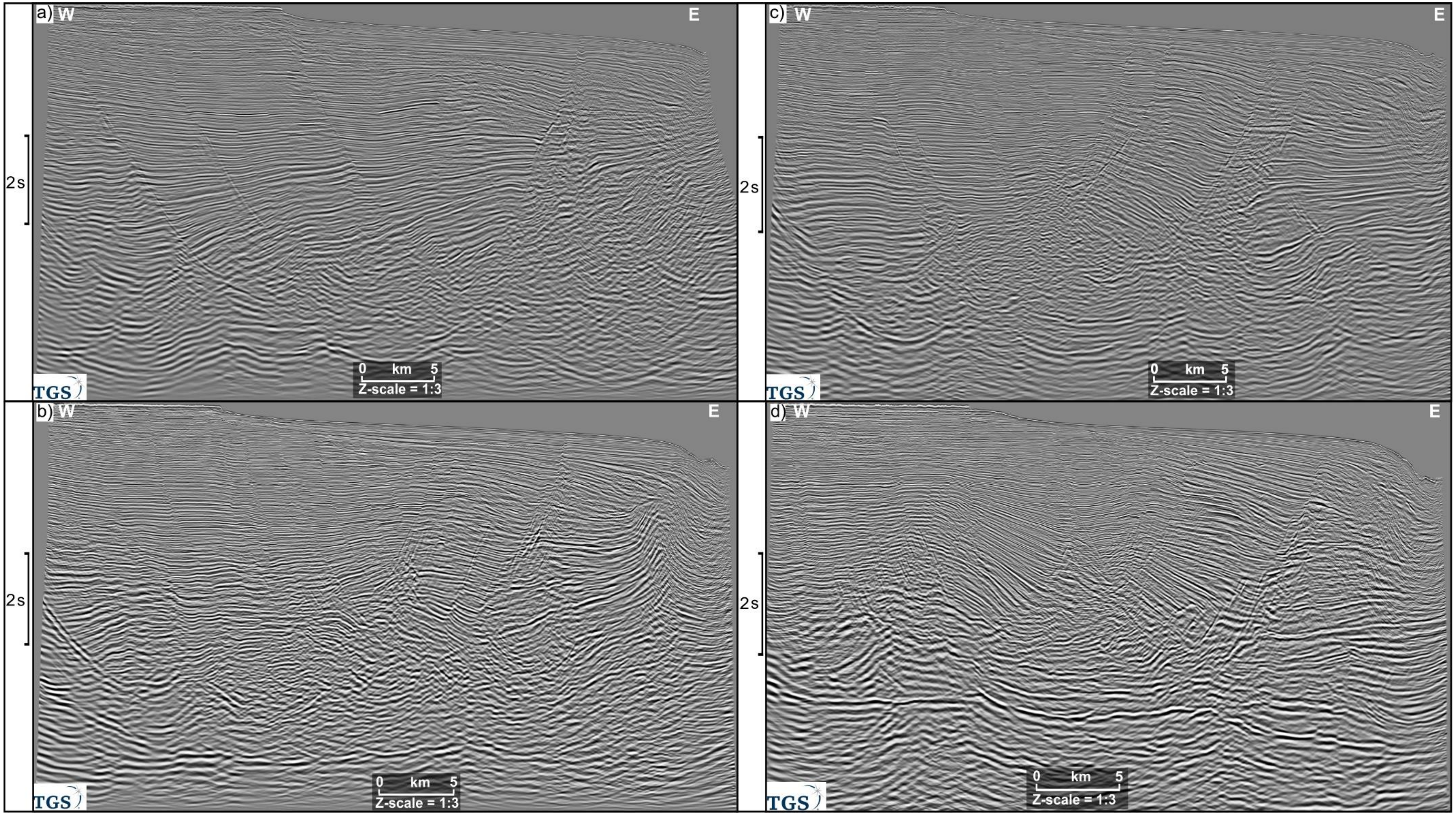

Figure S 2. (a-d) Uninterpreted margin-perpendicular (parallel to regional base-mobile shale and bulk translation direction) seismic profiles of figure 4 in main text across southern area.

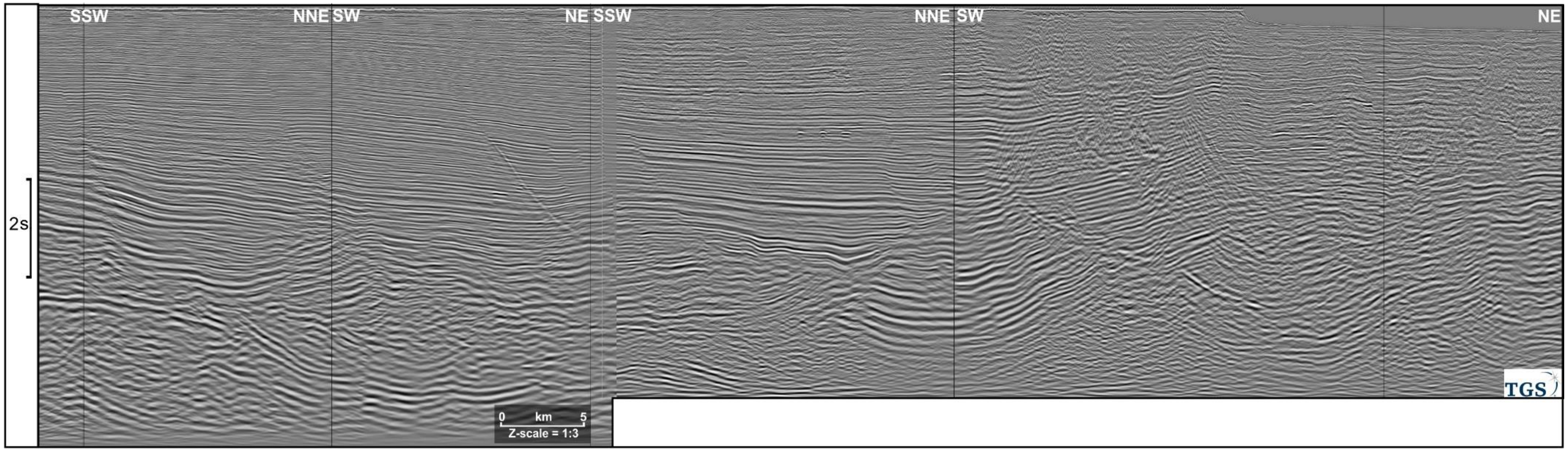

Figure S 3. Margin-parallel (i.e. normal to regional base-mobile shale and bulk translation direction) seismic profiles of figure 5 in main text.

Appendix S2. A large version of isopach and interpretative sketch maps

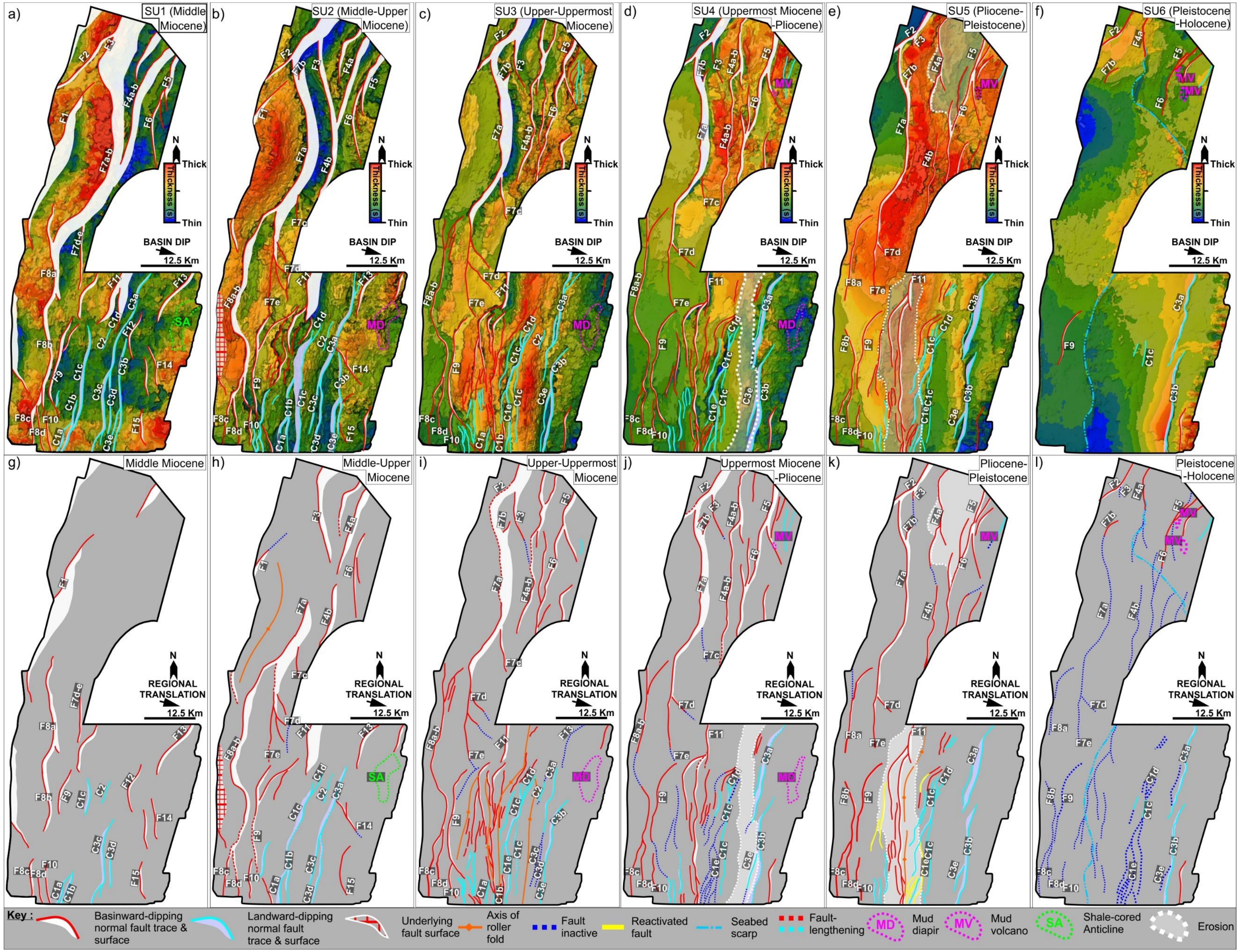

Figure S 4. (a-l) A larger version of figure 8 in main text, showing overburden isopach and their interpretative sketch maps that illustrate evolution of shale and supra-shale structures during Middle Miocene until Holocene.